Functioning human lung organoids model pulmonary tissue response from carbon nanomaterial exposures

Rahaf Issa[1, 2], Neus Lozano[3], Kostas Kostarelos[1, 2, 3] and Sandra Vranic[1, 2]*

[1] *Nanomedicine Lab, Faculty of Biology, Medicine and Health, The University of Manchester, Manchester, M13 9PT, U.K.*

[2] *National Graphene Institute, The University of Manchester, Booth Street East, Manchester, M13 9PL, U.K.*

[3] *Catalan Institute of Nanoscience and Nanotechnology (ICN2), CSIC and BIST, Campus UAB, Bellaterra, 08193 Barcelona, Spain.*

*Corresponding author: sandra.vranic@manchester.ac.uk

ABSTRACT

Human lung organoids (HLOs) are increasingly used to model development and infectious diseases, however their ability to recapitulate functional pulmonary tissue response to nanomaterials (NMs) has yet to be demonstrated. Here, we established a lung organoid exposure model that utilises microinjection to present NMs into the lumen of organoids. Our model assures efficient, reproducible and controllable exposure of the apical pulmonary epithelium, emulating real-life human exposure scenario. By comparing the impact of two well studied carbon-based NMs, graphene oxide sheets (GO) and multi-walled carbon nanotubes (MWCNT), we validated lung organoids as tools for predicting pulmonary NM-driven responses. In agreement with established *in vivo* data, we demonstrate that MWCNT, but not GO, elicit adverse effects on lung organoids, leading to a pro-fibrotic phenotype. Our findings reveal the capacity and suitability of HLOs for hazard assessment of NMs, aligned with the much sought-out 3Rs (animal research replacement, reduction, refinement) framework.

INTRODUCTION

The current standard for pulmonary tissue response analysis combines mono/co-culture *in vitro* systems[1,2], with time-intensive and ethically charged *in vivo* models[3-5]. Though mono/co-culture systems allow for large-scale screening of nanomaterials (NMs), and have provided a better understanding of cellular effects with regards to physicochemical features of NMs[2], such systems are often too simplistic. They lack physiological functions and only partially depict the complex cross-talk between cells. Such models also do not represent the complexity of human pulmonary epithelium and may overestimate the toxic potential of NMs. With *in vivo* models, ethical concerns and costs limit the number of NMs that can be evaluated. Furthermore, concerns regarding animal welfare, suitability and the accuracy of such models to predict human physiological responses have initiated much discussion around the use of animals in chemical safety testing, and the application of the 3Rs framework which aims to reduce, refine and replace animal testing[6].

In recent years, advanced three-dimensional *in vitro* cultures have grown in popularity[7]. Examples include *ex vivo* precision-cut lung slices, lung cell type spheroids, air-liquid interface cultures and microfluid lung-on-a-chip models[7]. Such platforms have provided a unique alternative to bridge the gap between traditional two-dimensional *in vitro* and *in vivo* models, but to date most consist of only two or three cell types[8-10]. It is therefore essential to develop a new approach that can accurately model NM-induced pulmonary tissue response in relatively short-term[11], providing sufficient cellular complexity and realistic NM-exposure scenario.

One of the most promising and emerging modelling technologies exploits the use of human organoid systems. Lung organoids are *in vitro,* self-organising, three-dimensional culture systems that are derived from either progenitor cells of the adult lung[12] or pluripotent stem cells[13,14]. They recapitulate key structures and functions of human tissue, making it possible to study developmental patterns and diseases[12,15]. To date, several groups have described the step-wise differentiation of human pluripotent stem cells into lung organoids containing proximal and/or distal airway cells[13,14,16-20]. In terms of application, lung organoids have been used to better understand various pulmonary diseases, from cystic fibrosis to lung cancer[12], and infectious diseases such as respiratory syncytial virus infection[14] and SARS-CoV-2 infection[21]. Several perspective articles have also discussed the potential usefulness of human organoids in toxicology and hazard assessments[22,23], with a focus on drug-induced organ toxicity in liver, heart, kidney, intestinal and brain organoids[22]. However, the ability of multilineage,

60 multicellular HLOs to recapitulate functional pulmonary tissue response to NMs has not yet
61 been demonstrated.

62 With the expansion of nanotechnology, there is a pressing need to understand how NMs may
63 impact human health. Inhalation of aerosolised materials is one of the first routes of exposure,
64 with the respiratory system first impacted. Previous *in vitro* and *in vivo* studies have shown
65 that some carbon nanotubes (CNTs) induce pulmonary-associated toxicity[9,24-28], with their
66 ability to biopersist in the lungs strongly influenced by their physicochemical properties
67 (length, diameter, aspect ratio and rigidity)[29]. Long multi-walled CNTs (MWCNT) have been
68 shown to induce adverse pulmonary effects, causing persistent inflammation[30], abnormal
69 deposition of extracellular matrix[31], formation of irreversible fibrotic lesions with tissue
70 remodelling[26], necrosis, and even carcinogenesis[32].

71 As a safer alternative, graphene oxide (GO) has emerged[33]. GO has fast become one of the
72 most studied two-dimensional NMs, mainly due to its ease of production, high surface area
73 exploitable for drug loading, and oxygen-rich functional groups that enable its good colloidal
74 dispersion in physiological *milieu*. Because of its similarity in chemical composition to other
75 carbon nanostructures, namely CNTs, efforts are made to evaluate the impact of GO on lungs
76 after inhalation[4,5,34,35]. Our group and others have previously shown that GO-induced toxicity
77 is strongly dependent on the lateral dimension of the material[1,2,36]. Micrometric-sized GO
78 sheets, when presented to rodent lung by a single intranasal aspiration, trigger granuloma
79 formation that persists for up to 90d, but this does not lead to pulmonary fibrosis[37]. In contrast,
80 nanometric-sized GO sheets are not associated with any adverse pulmonary effects[37,38]. More
81 recently, it was shown that murine lungs can rapidly recover from repeated low dose exposures
82 to micrometric GO sheets, despite initial signs of material-induced lung inflammation and
83 genotoxicity[4,5].

84 In this study, we used HLOs to evaluate NM-induced pulmonary responses, and assess their
85 suitability as a predicative tool in hazard assessment of carbon NMs. We adapted previously
86 published protocols to develop an embryonic stem cell-derived HLO, composed of six major
87 proximal and distal airway epithelial cells, and mesenchymal cells which are important for
88 modelling pulmonary fibrosis[15]. We established a novel NM microinjection protocol that
89 tailored the dosing of carbon-based NMs to the apical surface of lung organoids, hence
90 mimicking human pulmonary exposures. The impact of small (30-750nm, sGO) and large (11-
91 67µm, lGO) GO sheets in lateral dimension was compared with long and rigid MWCNT on

92 HLOs after 1d and 7d exposure. Key biological endpoints relevant to pulmonary tissue
93 response of carbon-based NMs[4,5,37] were investigated, including cytotoxicity, material-cell
94 interactions, tissue remodelling and pulmonary fibrosis.

95

96 **RESULTS**

97 **HLOs development and characterisation**. A multilineage and mature HLOs were established
98 by adapting previously published protocols **(Figure 1A)**[18,39]. The hESC line used in this study,
99 Man-5 **(Figure 1B)**, was maintained in a pluripotent state and exhibited a normal female
100 karyotype **(Figure S1)**. Differentiation of cells was verified at key stages; d4.5, d15 and d25.
101 At d4.5, >95% cells were $CXCR4^{+}cKIT^{+}$, markers of definitive endoderm **(Figure 1C)**. By
102 d15, 60% cells were epithelial ($EpCAM^{+}$) and co-expressed pre-AECII markers,
103 $MUC1^{+}PDPN^{+}$ **(Figure 1D)**. The purity of the lung progenitor cell population further increased
104 and at d25, >90% cells were $EpCAM^{+}$ with 28% expressing early AECII markers,
105 $MUC1^{+}PDPN^{-}$ **(Figure 1E)**. The protocol also yielded cultures that are highly enriched for the
106 expression of the endodermal marker FOXA2 and lung transcription factor NKX2.1, as well
107 as transcription factors SOX2 and SOX9 which are involved in proximodistal patterning of the
108 lung **(Figure 1F)**.

109 After maturation **(Figure 1G)**, HLOs exhibited an airspace-like lumen void of cells **(Figure**
110 **1H)**, that may be exploited for controlled NM exposures. Functional ciliated cells, which can
111 be seen beating when the organoid is dissociated into small cell clumps were identified **(Movie**
112 **1)**. Using immunofluorescence staining and TEM, the six major proximal and distal pulmonary
113 epithelial cell types were detected **(Figures 1I, S2)**. Consistent with the immunofluorescence
114 data, TEM showed the presence of goblet cells with secretory granules and ciliated cells
115 reaching the lumen **(Figure S2)**. Cells with electron-dense lamellar bodies, the functional
116 organelles in which surfactant is stored before exocytosis into the air spaces, were evident and
117 indicative of ACEII maturation. In some areas, surfactant deposition was also observed **(Figure**
118 **S2)**. These findings confirm the presence of functional proximal and distal airway cells in the
119 lung organoids.

120 **Lung organoid exposure model**. In the lung organoid, the apical surface of the epithelium is
121 enclosed while the basolateral surface faces the outside of the organoid **(Figure 1H)**. We
122 established a protocol to microinject controlled volume and dose of NMs into the lumen of the
123 organoid, simulating a real pulmonary exposure scenario of the apical region of the lung

124 epithelium **(Figure 2A)**. To control the amount of NM injected per organoid, we considered
125 the following parameters: organoid size, cell number per organoid, NM dose, volume injected
126 and vehicle. We first addressed the variation in organoid size in relation to the cell number per
127 organoid, as organoid development is hindered by the lack of size uniformity. Using FiJi image
128 analysis software, the size of 31 organoids was determined and ranged from 0.2 to 3.5 mm^2
129 **(Figure 2B)**. An excellent correlation between organoid size (measured by FiJi) and the actual
130 number of cells in each organoid (after dissociation into single cells) was observed, with R^2
131 value of 0.8654 **(Figure 2Bv)**. To assess if microinjection compromises the epithelial barrier
132 of the organoid, the retention of FD4 which is impermeable to intact membrane and
133 intracellular junctions was assessed **(Figure 2C)**. This also allowed us to evaluate whether the
134 injected cargo remains in the organoid lumen after needle withdrawal. Injections of up to 100
135 nl/mm^2 FD4 were retained by the organoids. However, increasing the volume to ≥200 nl/mm^2
136 resulted in a compromise in epithelial barrier function, as evidenced by leaching of the
137 fluorescent signal into surrounding matrix **(Figure 2C)**.

138 The NMs used were thoroughly characterized in water and in the vehicle used for
139 microinjections **(Figures S3-S4)**. To determine the NM dose to deliver into the organoids, we
140 considered the amount of material that deposits per cell *in vitro* **(Figure 2D)**, and the amount
141 of material administered in previous *in vivo* studies[37]. Further information can be found in
142 experimental subsection 'NM dosimetry in lung organoids'. Detailed schematic representation
143 of the study design is depicted in **Figure 2E**.

144 **MWCNT but not GO cause remodelling of the organoid epithelium**. Regardless of the NM
145 used, we observed a transient apoptotic effect in the lung organoids **(Figure S5-S6)**. However,
146 in organoids exposed to MWCNT, and not s/lGO, a significant reaction by the organoid
147 parenchyma was observed **(Figures 3, S7-S8)**. Cells within MWCNT-exposed organoids were
148 more densely packed with a distinctly thicker epithelium. Furthermore, the matrix appeared
149 more disorganised, particularly after 7d exposure **(Figures 3B, S7B, S8B)**. In areas of high
150 material load, there was significant damage to the epithelium as evidenced by the lack of
151 cellular integrity **(Figure 3B)**. Such organoids (MWCNT, 0.1 $\mu g/mm^2$) were challenging to
152 cryosection, as the nanotubes when present in high concentrations caused tissue damage
153 (dragging and tearing) on sectioning. To reduce mechanical-related damage, only organoids
154 exposed to ≤0.01 $\mu g/mm^2$ MWCNT were subsequently used.

155 **GO sheets interact less than MWCNT with alveolar cells.** The interaction of NMs with cells
156 can induce cellular responses that define the biological fate and toxicological profile of the
157 NM[1,2]. Interestingly, all three materials interacted with only distal airway cells, AECI and
158 ACEII **(Figures 4, 5)**. We did not observe any interaction with proximal airway cells **(Figures**
159 **S9-S11)**. However, the extent of cell interaction differed between materials. In organoids
160 exposed to s/lGO, the materials co-localised with HOPX and MUC1, markers of AECI and
161 ACEII respectively **(Figures 4A-4B)**, but this interaction was transient. After 7d exposure,
162 there was very limited cell-material interaction, but rather s/lGO was confined to regions of
163 secretory mucins (MUC1/MUC5AC). We compared the expression of secretory mucins and
164 surfactant in the NM-exposed organoids to the non-injected controls **(Figures 4C-4G)**.
165 Interestingly, there was a greater mucin production in response to lGO than sGO exposure
166 **(Figures 4A-4B, 4F)**. In organoids exposed to lGO, we observed a 2.1- and 1.8-fold increase
167 in MUC5AC and MUC1 expression, respectively **(Figure 4F)**. In contrast, sGO did not induce
168 mucin hypersecretion in the organoids **(Figures 4A, 4C)**, highlighting the importance of
169 nanosheet lateral dimension. The limited interaction of s/lGO with alveolar cells at 7d also
170 resulted in no alteration in the surfactant homeostasis of the lung organoids **(Figures 4D-4E,**
171 **4G)**. In contrast, MWCNT exposure induced a more persistent interaction with AECI/II cells
172 **(Figure 5A)**. Regardless of the exposure time, MWCNT remained localised to cells expressing
173 HOPX and MUC1. In these organoids, we did not observe any signs of mucin hypersecretion
174 but rather a 7.8-fold increase in surfactant SFTPB expression, a protein secreted by mature
175 ACEII **(Figures 5B-5C)**. Furthermore, in areas of high material load (indicated by a yellow
176 arrow in **Figure 5A**), cells stained for neither epithelial, proximal nor distal airway cells.

177 **MWCNT induce pulmonary fibrosis in the organoid after 7d exposure**. Persistent injury
178 to the alveolar epithelium is known to induce fibrosis, where AECII undergo epithelial-
179 mesenchymal transition (EMT) to repair the injured tissue[40,41]. Unlike Carvalho *et al.*[39], we
180 observed positive staining for markers of mesenchymal cells in HLOs, highlighting the
181 organoid's potential for modelling pulmonary fibrosis (**Figure 6A**, non-injected controls). To
182 assess if MWCNT interaction with AECI/II leads to fibrosis, we stained for epithelial and
183 mesenchymal markers. In organoids exposed to MWCNT for 7d, but not 1d, there was an
184 increased presence of cells expressing α-SMA (a member of actin family typically expressed
185 by fibroblasts) and vimentin (an intermediate filament and key biomarker of EMT), coupled
186 with a decrease in $EpCAM^+$ cells **(Figure 6A-C)**. These significant observations at d7 were

187 further confirmed by quantifying the fluorescence area in the images **(Figure 6D)**. Together,
188 this indicates the presence of a fibrotic phenotype induced by MWCNT exposure.

189

190 **DISCUSSION**

191 Advances in stem cell technology and *in vitro* pulmonary tissue culture systems have
192 stimulated the need for more reliable testing approaches, that predict adverse tissue responses
193 and hazard from NM exposures and align with the 3Rs framework[7]. Lung organoids, provide
194 a system which supports the co-existence of diverse cell types, an intrinsic dynamic
195 environment created by the presence of functional multi-ciliated and secretory cells, extensive
196 cell-cell, cell-matrix interactions, and tissue-like morphology[13,14,17,18]. Though HLOs have
197 been used to better understand various diseases[12,14,21], no studies have attempted to interrogate
198 the potential of functioning, multilineage HLOs as alternative modelling platforms for
199 materials hazard assessment.

200 In this study, we asked whether hESC-derived lung organoids can model NM-induced
201 pulmonary tissue responses and generate similar outcomes to established *in vivo* models. The
202 HLO development protocol recapitulates both proximal and distal airways in 50d[18,39] **(Figure**
203 **1I)**. Importantly, it generates functional multiciliated cells **(Movie 1)**, mucus-producing goblet
204 cells and surfactant-producing AECII cells **(Figure 1I)**, all crucial for creating a true-to-life
205 NM exposure scenario. The genome-wide expression signature of this multilineage organoid
206 also corresponds to adult lung[18]. In other protocols, the maturity of HLOs is either unreported
207 or equivalent to foetal lung[13,14]. We next established a novel NM microinjection protocol that
208 tailored the dose of carbon-based NMs to the apical surface of HLOs, hence mimicking human
209 pulmonary exposures **(Figure 2A-B)**. One group has previously sheared the organoids through
210 mechanical disruption before incubating with desired microparticles[42]. Though it is easier than
211 microinjection, this method risks high mechanical injury at the time of incubation, and
212 exposure of both apical and basolateral surfaces. Microinjection thus allowed us to gain access
213 into the lumen of each organoid and dose its apical surface with a variety of NMs accurately,
214 reproducibly and precisely, without the risk of mechanical injury-induced effects.

215 We selected two extensively studied carbon-based NMs, GO sheets[1,4,5,37] and MWCNT[8,24,26,27],
216 to validate our HLO exposure model. Thin GO sheets are known to induce minimal-to-transient
217 pulmonary toxicity *in vivo*[37], whilst MWCNT (Mitsui-7) have consistently been associated

218 with adverse pulmonary effects[27,30,41,43]. Regardless of the NM, we observed a transient
219 apoptotic effect in the lung organoids **(Figure S5)**. Interestingly, co-/tri-cultures have been
220 shown to be more resilient to NM exposure than mono-cultures[10]. This suggests that the
221 heterogenous cell population and 3D architecture of the organoid enhances the likelihood of
222 recovery post exposure, and further supports the notion that mono-cultures might overestimate
223 the response to NMs[14].

224 Regardless of the primary lateral dimension, sGO and lGO sheets formed agglomerates,
225 trapped in secretory mucins (MUC5AC/MUC1), within the organoid lumen after 7d exposure
226 **(Figures 4A-4B)**. Previous *in vivo* studies have shown that impact of graphene-based materials
227 is size-dependent[4,5,37], and that micrometric GO sheets do not translocate well into lungs and
228 are likely to undergo mucociliary clearance[37]. Indeed, we observed increased mucin production
229 in lGO-exposed organoids at d7 **(Figures 4C, 4F)**, suggesting that organoids can tailor the
230 mucin production to reduce damage to the epithelial surface and achieve sufficient mucociliary
231 clearance. Though only a small proportion of lGO sheets reaches the lungs *in vivo*[37], high
232 material reactivity has been previously reported. One factor that has been shown to reduce the
233 adverse biological impact of micrometric materials is protein coating[1]. Thus, the
234 overproduction of mucin in response to lGO and its entrapment in secretory mucin may explain
235 the lack of lGO-induced cytotoxicity in the organoids at d7 **(Figure S5B)**. In rodents, lGO but
236 not sGO exposure induces pulmonary granuloma formation, following the recruitment of
237 interstitial macrophages and dendritic cells[4,37]. This however resolves within 90d and does not
238 lead to fibrosis[37]. We were unable to model the formation of granuloma in response to lGO
239 exposure, as our organoids recapitulate the epithelial component of human lungs. But in
240 agreement with *in vivo* data, organoids exposed to GO did not exhibit any histopathological
241 changes **(Figures 3, S7-S8)**, or remodelling of the extracellular matrix indicative of fibrosis[37].
242 This further highlights the potential of organoids in predicting graphene-based material
243 toxicity.

244 In contrast to GO, MWCNT exposure caused significant remodelling of lung organoids
245 **(Figures 3B, S7B, S8B)**. CNTs are known to rapidly penetrate the alveoli and interstitial space
246 *in vivo*[29,40,44]. Indeed, we observed a persistent interaction of MWCNT with the alveolar
247 epithelium, coupled with limited mucin secretion suggesting a lack of mucociliary clearance
248 **(Figures 5A-5B)**. Persistent injury to the alveolar epithelium has previously been shown to
249 lead to lung fibrosis[37,41]. Consistent with *in vivo* data, MWCNT exposure for 7d induced EMT,

250 an indirect indicator of fibrinogenic activity of this NM, as demonstrated by an increase in cells
251 expressing mesenchymal markers coupled with a decrease in epithelial cell number **(Figure**
252 **6B)**.

253 Pulmonary injury such as fibrosis is also known to alter the homeostasis of the lung[37,41,45,46]. *In*
254 *vivo* studies have shown that inducing lung injury significantly elevates the surface tension of
255 the lung and/or surfactant SFTPB/C levels[45,46]. Indeed, in MWCNT-treated organoids we
256 observed a significant increase in the expression of SFTPB **(Figures 5A-5C)**, a pulmonary
257 surfactant important for decreasing the surface tension along the alveolar epithelium and
258 reducing alveolar collapse[47]. Exposure to a pro-fibrotic stimulus like MWCNT may have
259 increased the surface tension of the alveolar epithelium, prompting the surfactant-producing
260 cells in the organoid, AECII, to synthesise more SFTPB. This elevated surfactant level may be
261 an attempt to reduce the surface tension induced by fibrosis and repair the MWCNT-damaged
262 organoid. Alterations in surfactant homeostasis may also explain why organoids exposed to
263 MWCNT lacked a clear lumen, appearing more collapsed **(Figures 3A-4B, S7B-S8B)**.
264 Conversely, exposure to a non-fibrotic stimulus such as GO did not cause any changes in
265 surfactant SFTPB expression **(Figures 4D-4E, 4G)**. This observed consistency between the
266 histopathology and biochemistry endpoints suggests that our model is capable of detecting and
267 responding to pro-fibrotic nanomaterials, such as MWCNT, with relatively high sensitivity and
268 specificity.

269 The HLO exposure model presented here aligns well with the 3Rs framework, and has the
270 potential to bridge the gap between traditional 2D *in vitro* models, animals and humans in terms
271 of pulmonary tissue-responses. With further validation using other NMs, prolonged exposure
272 times, and the incorporation of the immune component, this model could significantly replace
273 of current 2D *in vitro* systems, and greatly reduce the need for *in vivo* inhalation studies in the
274 assessment of material pulmonary responses.

275

276

277

278

279

280 **EXPERIMENTAL**

281 **hESC maintenance.** Man-5 (Manchester University Embryonic Stem Cell Line 5,
282 RRID:CVCL_L193) were kindly provided by Professor Susan Kimber, University of
283 Manchester. Cells were cultured on growth factor-reduced Matrigel (Corning), in mTeSR1
284 medium (STEMCELL Technologies). Media was changed daily and cells were passaged every
285 5-6 days using 0.5 mM EDTA. Media was supplemented with 10 μM ROCK inhibitor Y-27632
286 (Tocris) for a maximum of 24 h after splitting. Cells were maintained in an undifferentiated
287 state at 37°C, 5% CO_2, and used between passage 19-28. Cells were tested for mycoplasma
288 contamination every 4 months. Karyotype was verified using Cell Guidance Systems Genetics
289 Service on fixed cells of P28 Man-5.

290 **Human lung organoid culture.** Protocol for generation of lung organoids was adapted from
291 Carvalho *et al.*[18,39]. All steps were carried out in serum-free differentiation (SFD) medium
292 consisting of IMDM/F12 (3:1) (Life Technologies), N2 and B27 supplements (Life
293 Technologies), 1% GlutaMax (Gibco), 1% penicillin-streptomycin (Sigma), 0.05% bovine
294 serum albumin (Gibco), with 50 μg/ml ascorbic acid (Sigma) and 0.4 μM monothioglycerol
295 (Sigma) added fresh. All growth factors were purchased from R&D systems, unless otherwise
296 stated. Cultures were maintained at 37°C, 5% CO_2. For induction of definitive endoderm, hESC
297 (3-10 cells/clump) were plated onto low-attachment 6-well plates (Corning) in SFD medium
298 supplemented with 10 μM Y-27632, 100 ng/ml activin A, 0.5 ng/ml BMP4 and 2.5 ng/ml
299 FGF2. Cells were cultured for 84 h and media was changed daily. Endoderm yield was
300 determined by the expression of CXCR4 and c-KIT, with cells used in all studies exhibiting
301 >95% endodermal yield. On day 4.5, embryoid bodies were dissociated into single cells using
302 0.05% trypsin/0.02% EDTA and plated onto fibronectin-coated plates (~60,000 cells/cm^2). For
303 induction of anterior foregut endoderm, cells were cultured in SFD medium supplemented with
304 10 μM SB431542 and 2 μM dorsomorphin dihydrochloride for 24 h, then switched to 10 μM
305 SB431542 and 1 μM IWP2 for a further 24 h. For induction of early-stage lung progenitor cells
306 (day 6-15), cells were exposed to SFD medium supplemented with 3 μM CHIR99021, 10 ng/ml
307 FGF7, 10 ng/ml FGF10, 10 ng/ml BMP4 and 50 nM all-trans retinoic acid (Sigma). Media was
308 changed every other day. On day 15, the early lung progenitors were briefly trypsinised, and
309 cell clumps (1-2 mm) were replated onto growth factor-reduced Matrigel-coated plates at a 1:2
310 split ratio. Cells were cultured in SFD medium supplemented with 3 μM CHIR99021, 10 ng/ml
311 FGF7 and 10 ng/ml FGF10 until day 25, with media changes every other day. For

312 differentiation of lung progenitors into organoids (day 25-50), cells were briefly trypsinised
313 and embedded in 4.5 mg/ml rat tail collagen I (Corning, Col I). Gels were allowed to set for 15
314 min, before SFD medium supplemented with 10 ng/ml FGF7, 10 ng/ml FGF10, 50 ng/ml
315 dexamethasone, 0.1 mM 8-bromo-cAMP and 0.1 mM IBMX was added. Media was changed
316 every other day.

317 **Material preparation.** Aqueous suspensions of small (s) and large (l) GO sheets were
318 produced in house as previously described[3]. Detailed characterisation of sGO and lGO can be
319 found in **Figure S3**. Optical image was acquired with a Nikon Eclipse LV100 microscope in
320 transmittance mode at a magnification of 50x, at the ICN2 Molecular Spectroscopy and Optical
321 Microscopy Facility. Electron microscopy images were obtained using a Magellan 400L field
322 emission scanning electron microscope (Oxford Instruments), at the ICN2 Electron
323 Microscopy Unit, with an Everhart–Thornley secondary electrons detector, using an
324 acceleration voltage of 20 kV and a beam current of 0.1 nA. Atomic force microscopy height
325 image was taken using an Agilent 5500 AFM/SPM microscope at the ICN2 Scanning Probe
326 Microscopy Facility, in tapping mode equipped with silicon cantilevers (Ted Pella) with a
327 nominal force of 40 N m−1 and a resonance frequency of 300 kHz. Multi-walled carbon
328 nanotubes (Mitsui-7, MWCNT) were a kind gift from Professor Ulla B Vogel, National
329 Research Centre for the Working Environment, Denmark. MWCNT were exposed to dry heat
330 sterilisation (160°C for at least 16 h) to inactivate any contaminating endotoxins. MWCNT
331 stock suspension was prepared in phosphate buffer saline without Ca^{2+} and Mg^{2+} (Sigma, PBS^{-}
332 $^{/-}$) containing 0.5% BSA and subjected to sonication for 5-7 min at nominal 80 W. GO and
333 MWCNT suspensions were diluted in $PBS^{-/-}$ and used immediately. All nanomaterials were
334 evaluated for endotoxin contamination as described in Mukherjee *et al.*[48] and tested negative
335 (data not shown).

336 **Microinjection of NMs.** Microcapillaries (3.5", Drummond) were prepared using the P-97
337 micropipette puller (Sutter) fitted with a 3.0 mm trough filament; with pressure set at 300, heat
338 at 295, velocity at 10 and delay at 250. Pulled capillaries were UV-sterilised for 20 min before
339 use. Only microneedles with a tip diameter between 8-21 μm were used in the study. Prior to
340 injections, organoids were gently transferred to an 8-well chamber slide (Ibidi) using a wide-
341 bore pipette tip (2-3 organoids/well). Fresh 4.5 mg/ml rat tail Col I was added to each well and
342 allowed to gel to prevent movement during injection. Organoids were then imaged using the
343 EVOS FL imaging system (Thermo Scientific) at 4x magnification. Organoid area was

344 measured using the image analysis software, FiJi (v2.9.0/1.53t). Images were converted to 8-
345 bit and threshold values were determined to cover the organoid surface area. The area (mm^2)
346 was determined using the 'Analyse Particles' function of FiJi. For studies assessing the
347 organoid epithelial barrier, 4kDa FITC-dextran (FD4, Sigma) was prepared at 2 mg/ml in PBS
348 and injected into the organoids at a volume of up to 400 nl/mm^2. Treatments (sGO, lGO,
349 MWCNT or $PBS^{-/-}$ vehicle control) were injected into the organoids, at a maximum volume of
350 100 nl/mm^2, using the Nanoject II microinjector (Drummond). To inject the airspace-like
351 lumen of the organoids, we used a diagonal needle approach. The microneedle was first
352 lowered on the organoid using a micromanipulator, and pressed down onto the organoid
353 surface. The needle tip was easily observed in the focal plane of the target organoid. The
354 microneedle was then moved laterally to pierce the organoid. The contents of the loaded
355 microneedle were injected into the organoid lumen. The microneedle was finally removed from
356 the organoid lumen, by moving up and laterally away. Successful injections into the luminal
357 space were confirmed by the slight expansion of the organoid upon injection. A minimum of 4
358 independent replicates, each containing 3 organoids were used.

359 **NM dosimetry in lung organoids.** To determine the NM dose to deliver into the organoids,
360 the amount of material that deposits per cell *in vitro,* which has been previously reported by
361 our group for sGO in human bronchial epithelial cells, BEAS-2B (see Figure S2 in Chen *et*
362 *al.*[2]), was considered. Using UV-VIS spectrometry, the deposition of sGO was calculated at
363 ~0.22 µg/10^4 cells after 24h incubation. The dose *in vivo* was also estimated to be ~0.1 µg/cm^2,
364 by taking into account the entire surface area of the respiratory tract of adult mouse (~500 cm^2)
365 and the amount of material administered (50 µg/mouse) in previous *in vivo* studies using the
366 same materials[37]. Thus, in the lung organoid exposure model here that contains 40,000
367 cells/mm^2, a high GO dose equated to 0.2 µg/mm^2, middle to 0.02 µg/mm^2 and low to 0.002
368 µg/mm^2. The volume injected (nl) was also adjusted based on the calculated organoid size
369 (mm^2) to prevent damage to the organoid's epithelial barrier, with maximum volumes set to
370 100 nl/mm^2. Different delivery vehicles, from cell culture media to physiological buffers, were
371 compared to identify a suitable vehicle for the NMs. $PBS^{-/-}$ was selected as sGO and lGO did
372 not show any major signs of agglomeration, even after 24h of preparation **(Figure S4)**. By
373 considering the following parameters: injection volume, organoid size, cell number per
374 organoid, NM dose and vehicle used – we could tailor NM delivery to each organoid. For
375 example, a 0.5 mm^2 organoid exposed to high dose sGO received 0.1 µg sGO in 50 nl $PBS^{-/-}$,
376 whereas a 3 mm^2 received 0.6 µg sGO in 300 nl $PBS^{-/-}$.

377 **Quantification of cell number per organoid.** Lung organoids in Col I gels were digested with
378 150 U/ml collagenase type I (Gibco, in IMDM) for 1 h at 37°C. Organoids were collected and
379 further dissociated with pre-warmed 0.05% trypsin/EDTA and gentle pipetting into single
380 cells. Cells were then counted using a haemocytometer. A total of 31 organoids, ranging
381 between 0.2 to 3.5 mm^2, were analysed.

382 **Histology.** Col I gels containing the lung organoid were embedded in Optical Cutting
383 Temperature (OCT) and snap-frozen in isopentane (Sigma) over dry ice. Serial sections were
384 obtained at 10 µm thick using a cryostat (Leica CM1950). Sections were either stained with
385 haematoxylin and eosin, using the XL autostainer (Leica Biosystems), or stored at -80°C for
386 immunostaining later. Brightfield images were acquired on a 3D-Histech Pannoramic-250
387 microscope slide scanner using a 20x/0.80 Plan Apochromat objective (Zeiss). Snapshots of
388 the slide-scans were processed using the Case Viewer software (3D-Histech).

389 **Immunofluorescence.** Sections were briefly fixed with 95% ethanol for 1 min followed by
390 4% paraformaldehyde (Thermo Scientific) for 15 min. After washing twice with PBS, sections
391 were permeabilised with 0.25% triton X-100 in blocking buffer (5% goat or donkey serum in
392 $PBS^{-/-}$) for 10 min, and then incubated with blocking buffer for 1 h. Primary antibodies (Table
393 S1) diluted in blocking buffer were incubated at 4°C overnight in a humidified chamber. The
394 following day, sections were washed with $PBS^{-/-}$ 3x5 min, incubated with the secondary
395 antibodies (Table S2, prepared in blocking buffer) for 2 h at room temperature followed by 10
396 min incubation with DAPI. Slides were again washed with $PBS^{-/-}$ 3x5 min and mounted using
397 Prolong Gold Antifade Mountant (Thermo Scientific). Sections stained with secondary only
398 antibodies were included to determine fluorescence threshold before image acquisition in each
399 channel. Images were acquired using Olympus BX63 upright microscope (20x 0.75 UApo/340
400 objective) and captured using a DP80 camera through CellSens Dimension software
401 (Olympus). Specific band pass filter sets for DAPI, FITC, Texas red and Cy5 were used to
402 prevent spectral bleed-through from one channel to the next.

403 For 2D cultures (hESCs or d25 lung progenitors), cells were fixed with only 4%
404 paraformaldehyde for 15 min prior to permeabilisation and staining. Images were acquired
405 using Zeiss LSM 780 confocal microscope (10x 0.50 Flar objective or 20x 0.8 Plan-
406 Apochromat objective, 1.5x confocal zoom).

407 For assessing cell-material interactions, organoid sections were stained for markers of proximal
408 and distal airway cells after exposure to s/lGO and MWCNT. Sequential organoid sections, 10
409 µm apart, were stained for the following cells types and markers; multiciliated (acTUB), goblet
410 (MUC5AC), club (SCGB1A1), basal (KRT5), AECI (HOPX), AECII (MUC1), secretory
411 mucins (MUC5AC/MUC1) and surfactant (SFTPB). Brightfield with immunofluorescence
412 images were overlayed to confirm the localisation of the materials, as they appear black/brown
413 under optical light.

414 **Quantification of immunofluorescence.** Images of each marker were quantified using the FiJi
415 software (v2.9.0/1.53t). Images were converted to 8-bit and the threshold was adjusted to
416 correspond to the nuclear stain, which allows for measurement of total area. For cytoplasmic
417 or membrane markers, the threshold was adjusted to cover the stained area. Fluorescent area
418 was analysed by the 'Analyse Particles' function of FiJi. Cells staining positive for each marker
419 were calculated by dividing the total area of positive cells over the total area of DAPI.

420 **Flow cytometry.** Cell colonies were dissociated with either StemPro accutase (Gibco) for 8
421 min (hESC) or TrypLE (Gibco) for 15 min (d15/25 lung progenitors) at 37°C. Cells were
422 collected and washed twice with FACS buffer (0.5% BSA and 2 mM EDTA in $PBS^{-/-}$). For
423 pluripotency assessment of extracellular markers, cells were incubated with unconjugated anti-
424 SSEA4 or anti-TRA-1-60 for 1 h on ice, followed by incubation with goat anti-mouse Alexa
425 Fluor 488 for 30 min on ice. For intracellular markers (Oct.4, Nanog and SOX2), cells were
426 fixed with 2% paraformaldehyde for 20 min and permeabilised with 0.1% triton X-100 (in
427 $PBS^{-/-}$) for 15 min before staining. Donkey anti-rabbit Alexa Fluor 488 (for Oct.4) and goat
428 anti-mouse Alexa Fluor 488 (for SOX2 and Nanog) were used to label the cells. Cells stained
429 with secondary only antibodies were also included for gating. For analysis of d15/25 lung
430 progenitors, cells were incubated with anti-EpCAM Alexa Fluor 488, anti-PDPN PE and anti-
431 MUC1 APC at 4°C for 45 min. Details for antibodies and dilutions used can be found in Table
432 S3. Cells were analysed on BD Fortessa or BD Fortessa X20 (BD Bioscience). Results were
433 analysed using Flowjo v10.2 software. Analysis was gated on live, doublet-excluded cells.

434 **Annexin V/propidium iodide staining.** After material exposure and digestion of Col I gels,
435 organoids were dissociated with pre-warmed 0.05% trypsin/EDTA and gentle pipetting into
436 single cells. The cell suspension was incubated with 10% FCS (Sigma) for 30 min to allow the
437 cell membrane to recover from trypsinisation and prevent false positive staining with Annexin
438 V (AV). Cells were then washed with ice-cold PBS. AV staining was performed according to

439 the manufacturer (Molecular Probes). Briefly, cells (≤1x10^5) were resuspended in 100 µl AV
440 binding buffer and stained with 3 µl AV-Alexa Fluor 488 conjugate for 15 min. Propidium
441 iodide (PI, Sigma) was added immediately before analysis at a final concentration of 1.5 µg/ml.
442 Cells were analysed on BD Fortessa X20 (BD Bioscience). Results were analysed using Flowjo
443 v10.2 software. Analysis was gated on doublet-excluded cells (gating strategy can be found in
444 **Figure S6A**).

445 **Live imaging.** Lung organoids in Col I gels were digested with 150 U/ml collagenase type I
446 (in IMDM) for 1 h at 37°C. Organoids were collected and further dissociated with pre-warmed
447 0.05% trypsin/EDTA and gentle pipetting to small sized cell clumps. Cell clumps were
448 resuspended in SFD medium containing 10 ng/ml FGF7, 10 ng/ml FGF10, 50 ng/ml
449 dexamethasone, 0.1 mM 8-bromo-cAMP and 0.1 mM IBMX, and plated in a CELLview
450 culture dish (Greiner). Live imaging was performed using an Olympus IX83 inverted
451 microscope (60x 0.70LUC PlanFL N UIS 2 (Ph2) objective) equipped with an Orca ER camera
452 (Hamamatsu) through CellSens software (Olympus).

453 **Transmission electron microscopy.** Col I gel-free organoids were fixed with 4% PFA and
454 2.5% glutaraldehyde in 0.1 M HEPES buffer (pH 7.2) for at least 2 h, and post-fixed with
455 ferrocyanide reduced osmium. Organoids were dehydrated in increasing concentrations of
456 ethanol (30-100%) and in 100% acetone, before embedding in TAAB LV resin and
457 polymerisation at 60°C (>24 h). Ultrathin sections (70 nm) were cut with a diamond knife
458 (Diatome) and mounted on copper grids. Organoids were examined using a Talos L120C
459 electron microscope (Thermo Fisher).

460 **Statistical analysis.** Data were analysed using GraphPad Prism 9 (GraphPad Software Inc).
461 For multiple group comparisons, one- or two-way ANOVA was performed followed by
462 Dunnett or Tukey tests. Where appropriated, unpaired two-tailed Student's t-test was
463 performed. $P<0.05$ was considered statistically significant.

464

465

466

467

ACKNOWLEDGMENTS

This work was supported by the GrapheneFlagship project, H2020-FET-GrapheneCore3-#881603. The authors would like to acknowledge Dr Luis M. Arellano and Angeliki Karakasidi for the synthesis of GO materials, and Irene Rebollido for her contribution in the preparation of sGO. Also, we would like to thank Dr Nerea Murillo-Cremaes, Despoina Despotopoulou and Noelia Hernández-Lobato for their contributions to the characterisation of sGO and lGO. The ICN2 is funded by the CERCA programme, Generalitat de Catalunya, and is supported by the Severo Ochoa Centres of Excellence programme by the Spanish Research Agency (AEI, grant no. SEV-2017-0706). At the Faculty of Biology, Medicine and Health (University of Manchester), the authors would like to thank the following Core Facility staff for their expert advice and assistant: Dr Peter March and Dr Roger Meadows (Bioimaging Facility), Dr Aleksandr Mironov (Electron Microscopy Facility), Grace Bako and Joel Rigg (Histology Facility), and Dr Gareth Howell (Flow Cytometry Facility). The Bioimaging Facility microscopes and Histology Facility equipment used in this study were purchased with grants from UKRI Biotechnology and Biological Sciences Research Council, The Wellcome Trust and The University of Manchester Strategic Fund. The EM Core Facility (SCR_021147) microscope was purchased with an equipment grant from The Wellcome Trust.

CONFLICTS OF INTEREST

The authors declare no conflicts of interest.

AUTHOR CONTRIBUTIONS

SV conceived and supervised the work. RI and SV designed the experiments. RI established HLOs, developed the protocol for microinjection, performed all the exposures of HLOs to NMs and analysed all the results. NL produced and characterized GO. KK supervised preparation and characterization of GO. Manuscript was written and edited by RI, SV and KK, with the input from NL.

496 **REFERENCES**

497 1. Vranic S *et al.* Live imaging of label-free graphene oxide reveals critical factors causing
498 oxidative-stress-mediated cellular responses. *ACS Nano* **12**, 1373-1389 (2018).
499 2. Chen Y *et al.* Dynamic interactions and intracellular fate of label-free, thin graphene oxide
500 sheets within mammalian cells: Role of lateral sheet size. *Nanoscale Advances* **3**, 4166-
501 4185 (2021).
502 3. Rodrigues AF *et al.* A blueprint for the synthesis and characterisation of thin graphene
503 oxide with controlled lateral dimensions for biomedicine. *2D Materials* **5**, 035020 (2018).
504 4. Loret T *et al.* Innate but not adaptive immunity regulates lung recovery from chronic
505 exposure to graphene oxide nanosheets. *Advanced Science* **9**, 2104559 (2022).
506 5. de Luna LAV *et al.* Lung recovery from DNA damage induced by graphene oxide is
507 dependent on size, dose and inflammation profile. *Part Fibre Toxicol* **19**, 62 (2022).
508 6. Burden N *et al.* The 3Rs as a framework to support a 21st century approach for nanosafety
509 assessment. *Nano Today* **12**, 10-13 (2017).
510 7. Moreira A *et al.* Advanced *in vitro* lung models for drug and toxicity screening: The
511 promising role of induced pluripotent stem cells. *Advanced Biology* **6**, 2101139 (2022).
512 8. Barosova H *et al.* An *in vitro* lung system to assess the proinflammatory hazard of carbon
513 nanotube aerosols. *Int J Mol Sci* **21** (2020).
514 9. Kabadi PK *et al.* A novel human 3D lung microtissue model for nanoparticle-induced cell-
515 matrix alterations. *Part Fibre Toxicol* **16**, 15 (2019).
516 10. Camassa LMA *et al.* Advanced respiratory models for hazard assessment of
517 nanomaterials-performance of mono-, co- and tricultures. *Nanomaterials (Basel)* **12**
518 (2022).
519 11. Punt A *et al.* New approach methodologies (NAMs) for human-relevant biokinetics
520 predictions: Meeting the paradigm shift in toxicology towards an animal-free chemical
521 risk assessment. *ALTEX* **37**, 607-622 (2020).
522 12. Sachs N *et al.* Long-term expanding human airway organoids for disease modeling. *EMBO*
523 *J* **38** (2019).
524 13. Dye BR *et al. In vitro* generation of human pluripotent stem cell derived lung organoids.
525 *Elife* **4** (2015).
526 14. Chen YW *et al.* A three-dimensional model of human lung development and disease from
527 pluripotent stem cells. *Nat Cell Biol* **19**, 542-549 (2017).
528 15. Strikoudis A *et al.* Modeling of fibrotic lung disease using 3D organoids derived from
529 human pluripotent stem cells. *Cell Rep* **27**, 3709-3723 e3705 (2019).
530 16. McCauley KB *et al.* Efficient derivation of functional human airway epithelium from
531 pluripotent stem cells via temporal regulation of Wnt signaling. *Cell Stem Cell* **20**, 844-
532 857 e846 (2017).
533 17. Miller AJ *et al.* Generation of lung organoids from human pluripotent stem cells *in vitro*.
534 *Nat Protoc* **14**, 518-540 (2019).
535 18. de Carvalho ALRT *et al.* Glycogen synthase kinase 3 induces multilineage maturation of
536 human pluripotent stem cell-derived lung progenitors in 3D culture. *Development* **146**
537 (2019).
538 19. Jacob A *et al.* Differentiation of human pluripotent stem cells into functional lung alveolar
539 epithelial cells. *Cell Stem Cell* **21**, 472-488 e410 (2017).
540 20. McCauley KB *et al.* Single-cell transcriptomic profiling of pluripotent stem cell-derived
541 SCGB3A2+ airway epithelium. *Stem Cell Reports* **10**, 1579-1595 (2018).
542 21. Han Y *et al.* Identification of SARS-CoV-2 inhibitors using lung and colonic organoids.
543 *Nature* **589**, 270-275 (2021).

544 22. Matsui T & Shinozawa T. Human organoids for predictive toxicology research and drug
545 development. *Front Genet* **12**, 767621 (2021).
546 23. Mahapatra C *et al.* Emerging role and promise of nanomaterials in organoid research. *Drug*
547 *Discov Today* **27**, 890-899 (2022).
548 24. Polimeni M *et al.* Multi-walled carbon nanotubes directly induce epithelial-mesenchymal
549 transition in human bronchial epithelial cells via the TGF-beta-mediated Akt/GSK-
550 3beta/SNAIL-1 signalling pathway. *Part Fibre Toxicol* **13**, 27 (2016).
551 25. Ma-Hock L *et al.* Inhalation toxicity of multiwall carbon nanotubes in rats exposed for 3
552 months. *Toxicol Sci* **112**, 468-481 (2009).
553 26. Mercer RR *et al.* Pulmonary fibrotic response to aspiration of multi-walled carbon
554 nanotubes. *Part Fibre Toxicol* **8**, 21 (2011).
555 27. Porter DW *et al.* Acute pulmonary dose-responses to inhaled multi-walled carbon
556 nanotubes. *Nanotoxicology* **7**, 1179-1194 (2013).
557 28. Rahman L *et al.* Multi-walled carbon nanotube-induced genotoxic, inflammatory and pro-
558 fibrotic responses in mice: Investigating the mechanisms of pulmonary carcinogenesis.
559 *Mutat Res Genet Toxicol Environ Mutagen* **823**, 28-44 (2017).
560 29. Vietti G *et al.* Mechanisms of lung fibrosis induced by carbon nanotubes: Towards an
561 Adverse Outcome Pathway (AOP). *Part Fibre Toxicol* **13**, 11 (2016).
562 30. Hamilton RF *et al.* Effect of MWCNT size, carboxylation, and purification on *in vitro* and
563 *in vivo* toxicity, inflammation and lung pathology. *Part Fibre Toxicol* **10**, 57 (2013).
564 31. Wang P *et al.* Multiwall carbon nanotubes mediate macrophage activation and promote
565 pulmonary fibrosis through TGF-β/Smad signaling pathway. *Small* **9**, 3799-3811 (2013).
566 32. Kasai T *et al.* Lung carcinogenicity of inhaled multi-walled carbon nanotube in rats. *Part*
567 *Fibre Toxicol* **13**, 53 (2016).
568 33. Bussy C *et al.* Safety considerations for graphene: Lessons learnt from carbon nanotubes.
569 *Acc Chem Res* **46**, 692-701 (2013).
570 34. Fadeel B *et al.* Safety assessment of graphene-based materials: Focus on human health and
571 the environment. *ACS Nano* **12**, 10582-10620 (2018).
572 35. Bengtson S *et al.* Differences in inflammation and acute phase response but similar
573 genotoxicity in mice following pulmonary exposure to graphene oxide and reduced
574 graphene oxide. *PLoS One* **12**, e0178355 (2017).
575 36. Hu CX *et al.* Effects of lateral size, thickness, and stabilizer concentration on the
576 cytotoxicity of defect-free graphene nanosheets: Implications for biological applications.
577 *ACS Appl Nano Mater* **5**, 12626-12636 (2022).
578 37. Rodrigues AF *et al.* Size-dependent pulmonary impact of thin graphene oxide sheets in
579 mice: Toward safe-by-design. *Adv Sci (Weinh)* **7**, 1903200 (2020).
580 38. Ma J *et al.* Crucial role of lateral size for graphene oxide in activating macrophages and
581 stimulating pro-inflammatory responses in cells and animals. *ACS Nano* **9**, 10498-10515
582 (2015).
583 39. de Carvalho ALRT *et al.* The *in vitro* multilineage differentiation and maturation of lung
584 and airway cells from human pluripotent stem cell-derived lung progenitors in 3D. *Nat*
585 *Protoc* **16**, 1802-1829 (2021).
586 40. Wang P *et al.* Multiwall carbon nanotubes directly promote fibroblast-myofibroblast and
587 epithelial-mesenchymal transitions through the activation of the TGF-β/Smad signaling
588 pathway. *Small* **11**, 446-455 (2015).
589 41. Dong J *et al.* Pathologic and molecular profiling of rapid-onset fibrosis and inflammation
590 induced by multi-walled carbon nanotubes. *Arch Toxicol* **89**, 621-633 (2015).
591 42. Winkler AS *et al.* Human airway organoids and microplastic fibers: A new exposure model
592 for emerging contaminants. *Environment International* **163**, 107200 (2022).

593 43. Knudsen KB *et al.* Physicochemical predictors of multi-walled carbon nanotube-induced
594 pulmonary histopathology and toxicity one year after pulmonary deposition of 11 different
595 multi-walled carbon nanotubes in mice. *Basic Clin Pharmacol Toxicol* **124**, 211-227
596 (2019).
597 44. Mercer RR *et al.* Distribution and persistence of pleural penetrations by multi-walled
598 carbon nanotubes. *Part Fibre Toxicol* **7**, 28 (2010).
599 45. Mahavadi P *et al.* Altered surfactant homeostasis and alveolar epithelial cell stress in
600 amiodarone-induced lung fibrosis. *Toxicological Sciences* **142**, 285-297 (2014).
601 46. Horiuchi T *et al.* Increased surface tension of the lung and surfactant in bleomycin-induced
602 pulmonary fibrosis in rats. *Am J Respir Crit Care Med* **154**, 1002-1005 (1996).
603 47. Wasnick R *et al.* Notch1 Induces Defective Epithelial Surfactant Processing and
604 Pulmonary Fibrosis. *Am J Respir Crit Care Med* (2022).
605 48. Mukherjee SP *et al.* Detection of endotoxin contamination of graphene based materials
606 ssing the TNF-α expression test and guidelines for endotoxin-free graphene oxide
607 production. *PLOS ONE* **11**, e0166816 (2016).

608

609

610

611

612

613

614

615

616

617

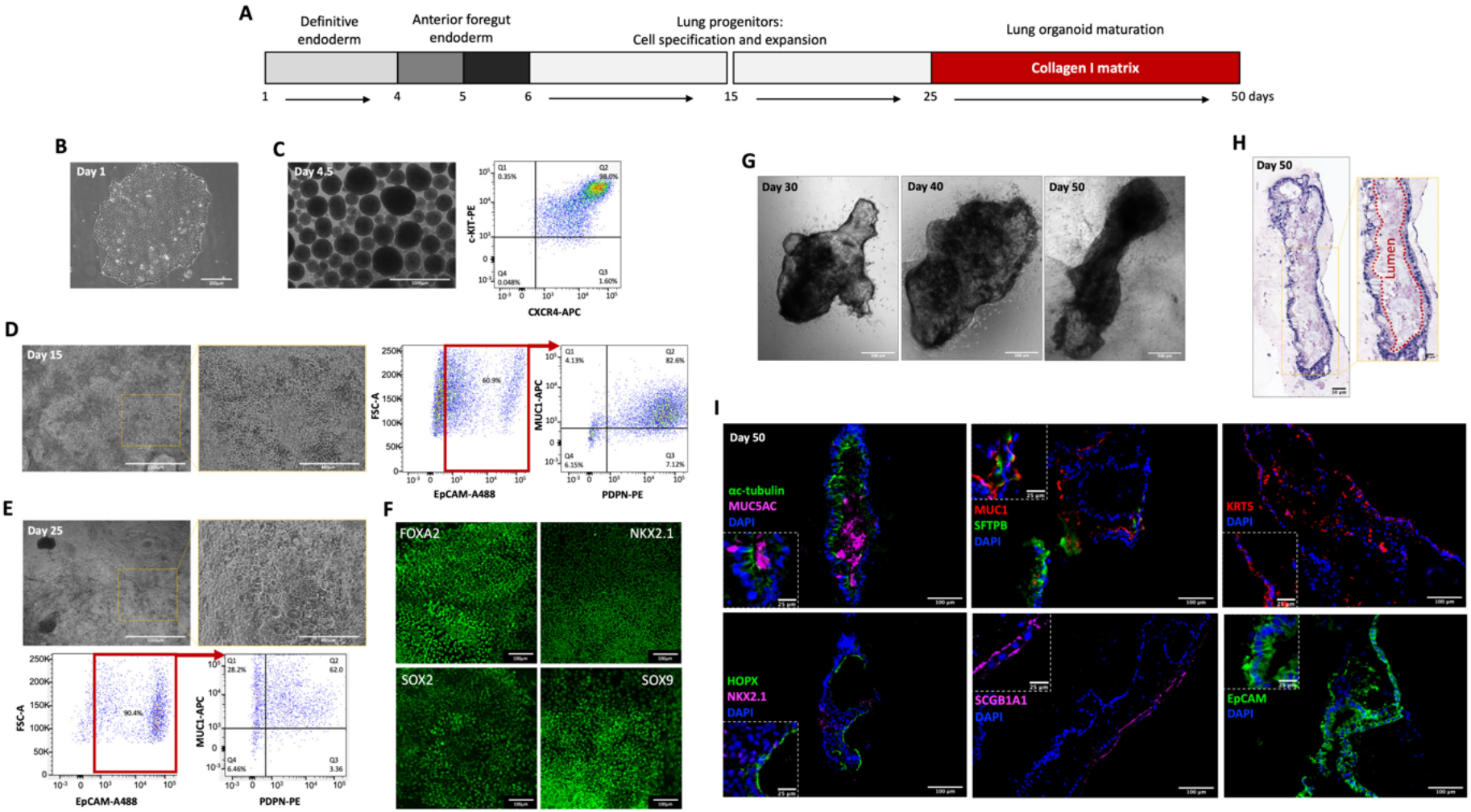

Figure 1. Generation of multilineage lung organoids from human embryonic stem cells (hESCs). A, Schematic representation of the differentiation protocol, adapted from Carvahlo *et al.*[39], from day 1 to 50. **B,** Brightfield image of hESC line Man5 after culturing to confluence. Scale bar, 200µm. **C,** Brightfield image of definitive endoderm at day 4.5, and a representative example of the flow cytometry profile after staining at day 4.5 cells for markers of definitive endoderm, CXCR4 and cKIT. Scale bar, 1000µm. **D-E**, Brightfield images of day 15 **(D)** and day 25 **(E)** of lung progenitors. Cell population profile after staining at day 15 (**D**) and day 25 (**E**) lung progenitor cells for EpCAM, and markers of pre- or mature- alveolar cells, PDPN and MUC1, respectively. Scale bar, 1000µm (Inset, 400µm). **F**, Immunofluorescence micrographs of day 25 lung progenitors expressing markers of lung lineage, FOXA2, NKX2.1, SOX2 and SOX9. Scale bar, 100µm. **G**, Brightfield image of developing lung organoids at day 30, 40 and 50. Scale bar, 500µm. **H**, H&E staining of a day 50 lung organoid (cryo-sectioned, 6µm slices). Scale bar, 50µm (Inset, 20µm). **I**, Immunofluorescence micrographs of day 50 lung organoid sections expressing markers of proximal and distal airway epithelial cells. Multiciliated cells (ac-tubulin), goblet (MUC5AC), club (SCGBA1A), basal (KRT5), AECI (HOPX), AECII (MUC1, SFTPB), and lung epithelium (EpCAM). Scale bar, 100µm (Inset, 25µm). FSC-A, forward scatter area. A488, Alexa-fluor 488. PE, phycoerythrin. APC, allophycocyanin.

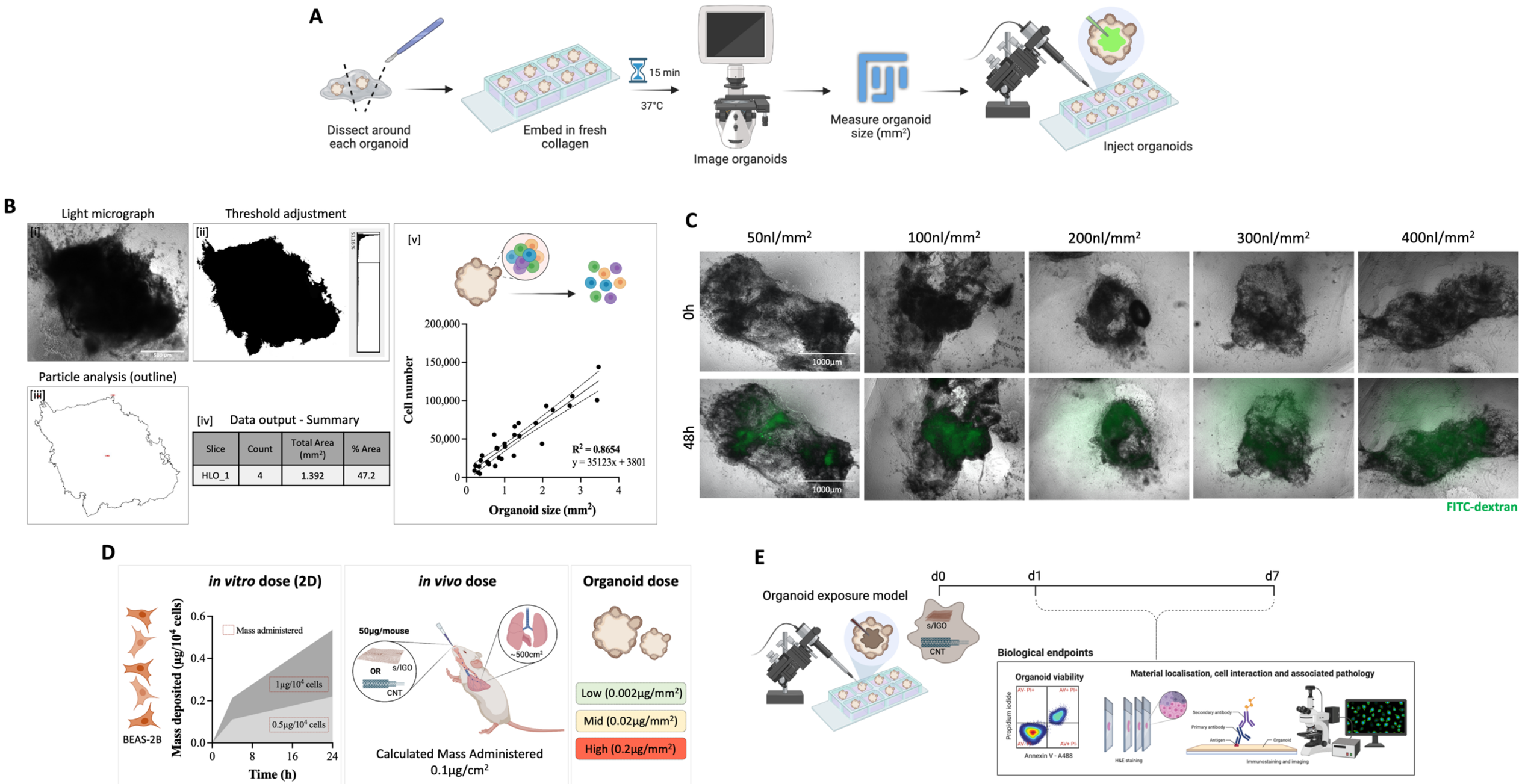

Figure 2. Microinjection of human lung organoids. A, Experimental set-up for cargo delivery into lung organoids. **B,** Correlation between organoid size (measured using the FiJi image analysis software [i-iv]) and total cell number [v], after organoids are dissociated into single cells. **B[i],** Light micrograph of a lung organoid. **B[ii],** After threshold adjustment in FiJi. **B[iii],** Organoid outline generated using the 'Analyse Particles' function in FiJi. **B[iv],** Summary of the data output detailing organoid size (mm^2). Scale bar, 500 µm. **C,** Microinjection of varying volumes of FITC-dextran in lung organoids, before (0h) and after (48h) injection. Both panels show events under the GFP filter merged with brightfield. n = 2 organoids per condition. Scale bar, 1000 µm. **D,** Mass deposition reported *in vitro* for sGO on human lung epithelial cells, BEAS-2B, after 24h of exposure[2], *in vivo* for s/lGO and MWCNT in an adult C57BL/6 mouse model after intranasal instillation[3], and the concentrations of GO injected into human lung organoids. **E,** Schematic representation of the study design. Organoids were microinjected with sGO, lGO or MWCNT and exposed to the materials for 1d and 7d. The impact of material exposure on lung organoids was assessed by investigating key biological endpoints relevant to pulmonary toxicity of carbon-based NMs, which included cytotoxicity, material-cell interaction, tissue remodelling and pulmonary fibrosis.

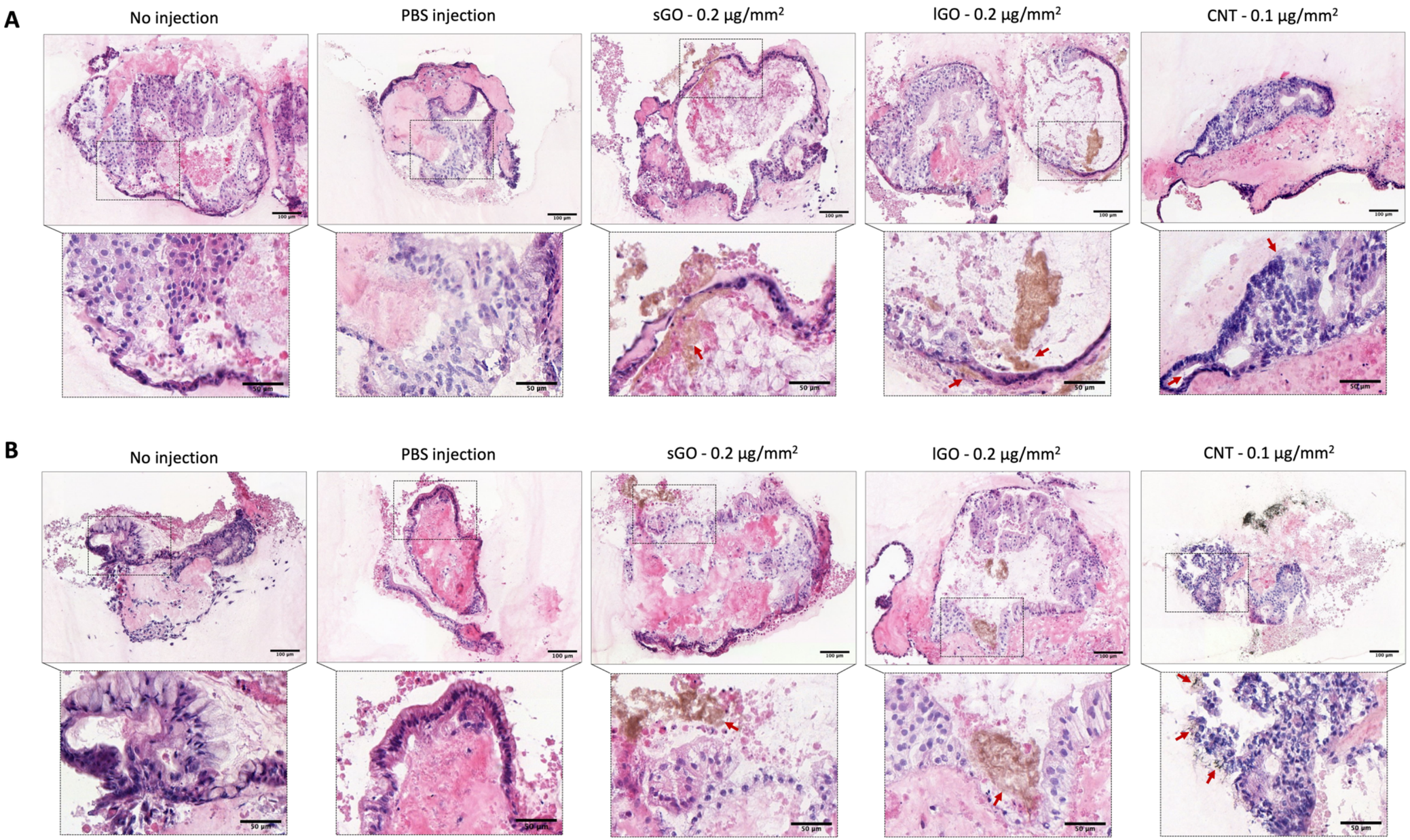

Figure 3. Histological analysis of human lung organoids after 1d and 7d exposure to high dose of carbon-based NM. A, 1d exposure. **B,** 7d exposure. Organoids were flash-frozen, cryo-sectioned at a thickness of 10 µm and stained with H&E. Arrows indicate material localisation. Scale bar, 100 µm (Inset, 50 µm). All three NMs were easily located in various regions of the organoids, appearing as brown (for GO) and black (for MWCNT) regions associated with the cells, extracellular matrix or secretory proteins in the luminal space. Histological analysis of lung organoids exposed to low- and mid-dose carbon-based NM are shown in Figure S7 and S8, respectively.

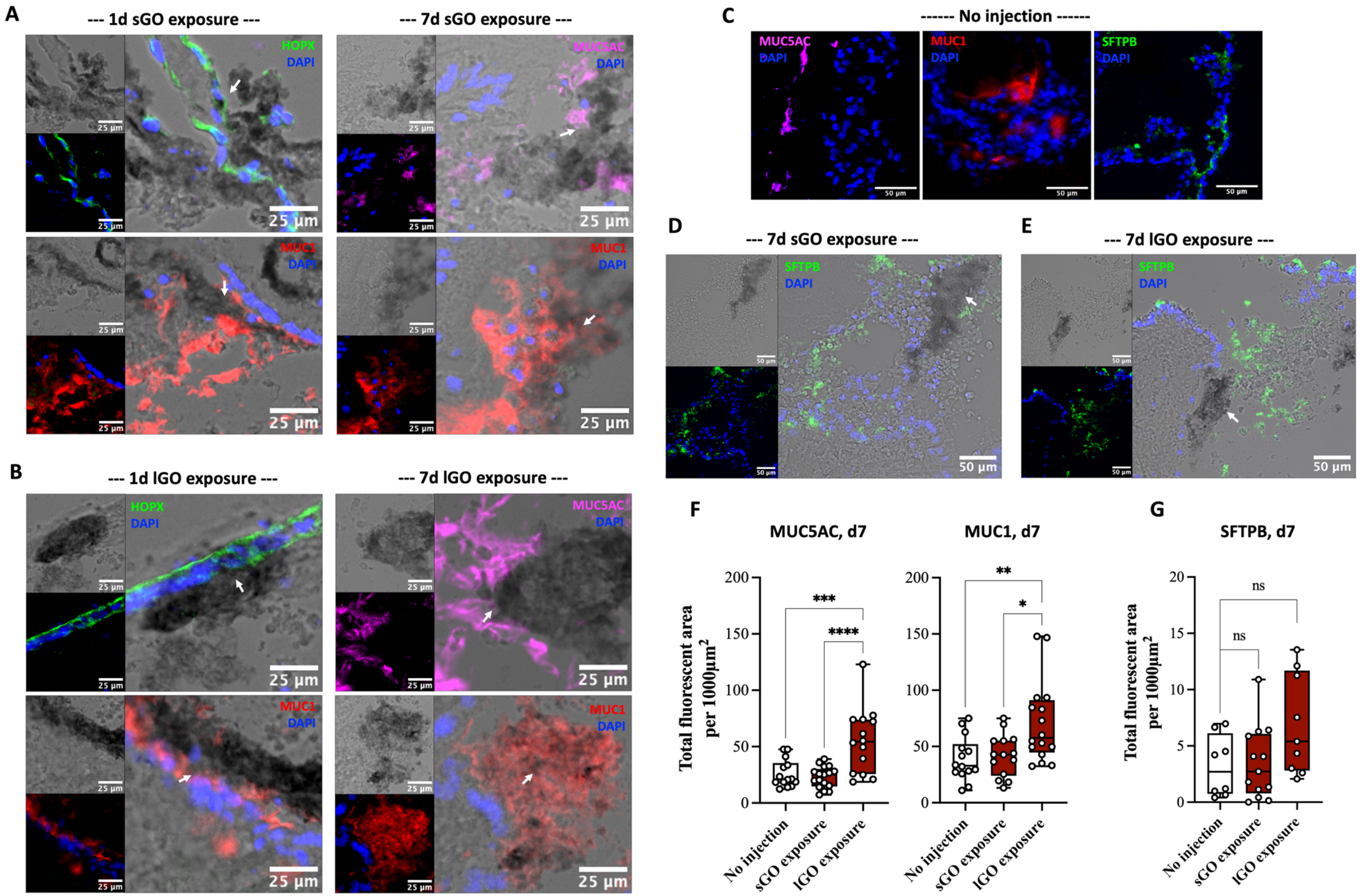

Figure 4. Interaction of sGO and lGO with alveolar cells, secreted mucins and surfactant in lung organoids. A, sGO exposure. **B,** lGO exposure. After material exposure, organoids were cryo-sectioned at thickness of 10 µm and immuno-stained for markers of proximal and distal airway epithelial cells. s/lGO dose, 0.2 µg/mm². HOPX (marker for AECI cells); MUC1 (marker for AECII cells when associated to organoid epithelium, or secretory mucin when present in the luminal space); MUC5AC (goblet cells when associated to organoid epithelium, or secretory mucin when present in the luminal space); DAPI (cell nucleus). Arrows indicate material localisation. Scale bar, 25 µm. **C,** Mucin (MUC5AC, MUC1) and surfactant (SFTPB) secretion in the non-injected controls. Scale bar, 50 µm. **D-E,** Surfactant secretion in response to sGO **(D)** and lGO **(E)** exposure for 7d. Scale bar, 50 µm. **F-G,** Semi-quantitative analysis showing the change in mucin (MUC5AC, MUC1) and surfactant (SFTPB) secretion after 7d exposure. Boxplots represent the median, with whiskers indicating minimum and maximum of data (n = 8 to 17 independent images, from 3 experiments). One-way ANOVA $*P < 0.05$, $**P < 0.01$, $***P < 0.001$, $****P < 0.0001$.

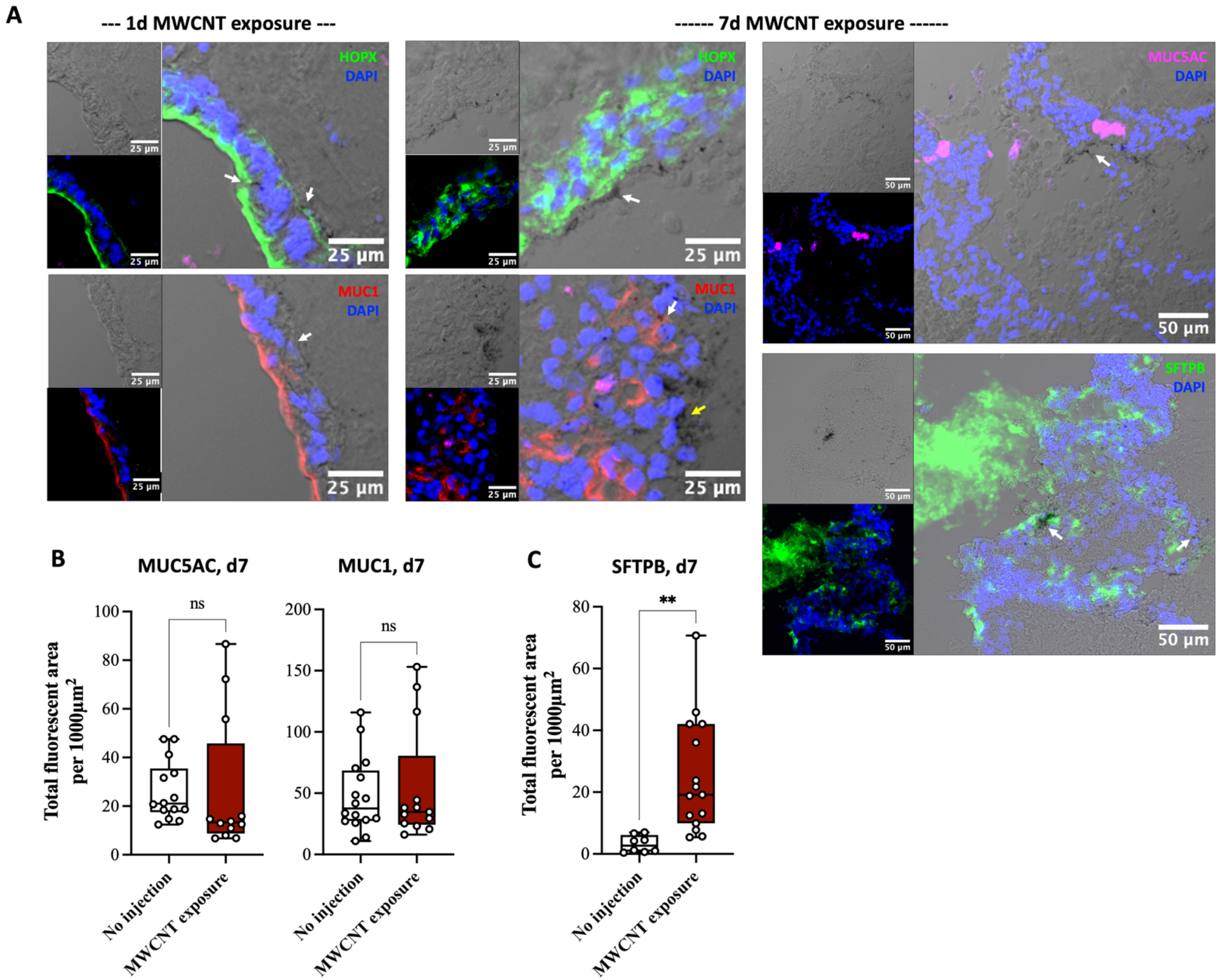

Figure 5. Interaction of MWCNT with alveolar cells, secreted mucins and surfactant in lung organoids. A, 1d and 7d exposure to MWCNT. After material exposure, organoids were cryo-sectioned at thickness of 10 µm and immuno-stained for markers of proximal and distal airway epithelial cells. MWCNT dose, 0.01 µg/mm^2. Organoids exposed to a mid dose of MWCNT were used to assess material-cell interaction due to the detrimental impact of MWCNT on the organoid, when sectioning at high material load. HOPX (marker for AECI cells); MUC1 (marker for AECII cells when associated to organoid epithelium, or secretory mucin when present in the luminal space); MUC5AC (goblet cells when associated to organoid epithelium, or secretory mucin when present in the luminal space); SFTPB (marker for surfactant protein B produced by AECII); DAPI (cell nucleus). Arrows indicate material localisation. **B-C,** Semi-quantitative analysis showing the change in mucin (MUC5AC, MUC1) and surfactant (SFTPB) secretion after 7d exposure. Boxplots represent the median, with whiskers indicating minimum and maximum of data (n = 8 to 16 independent images, from 3 experiments). Unpaired two-tailed Student's t-test. ns = not significant, $^{**}P < 0.01$.

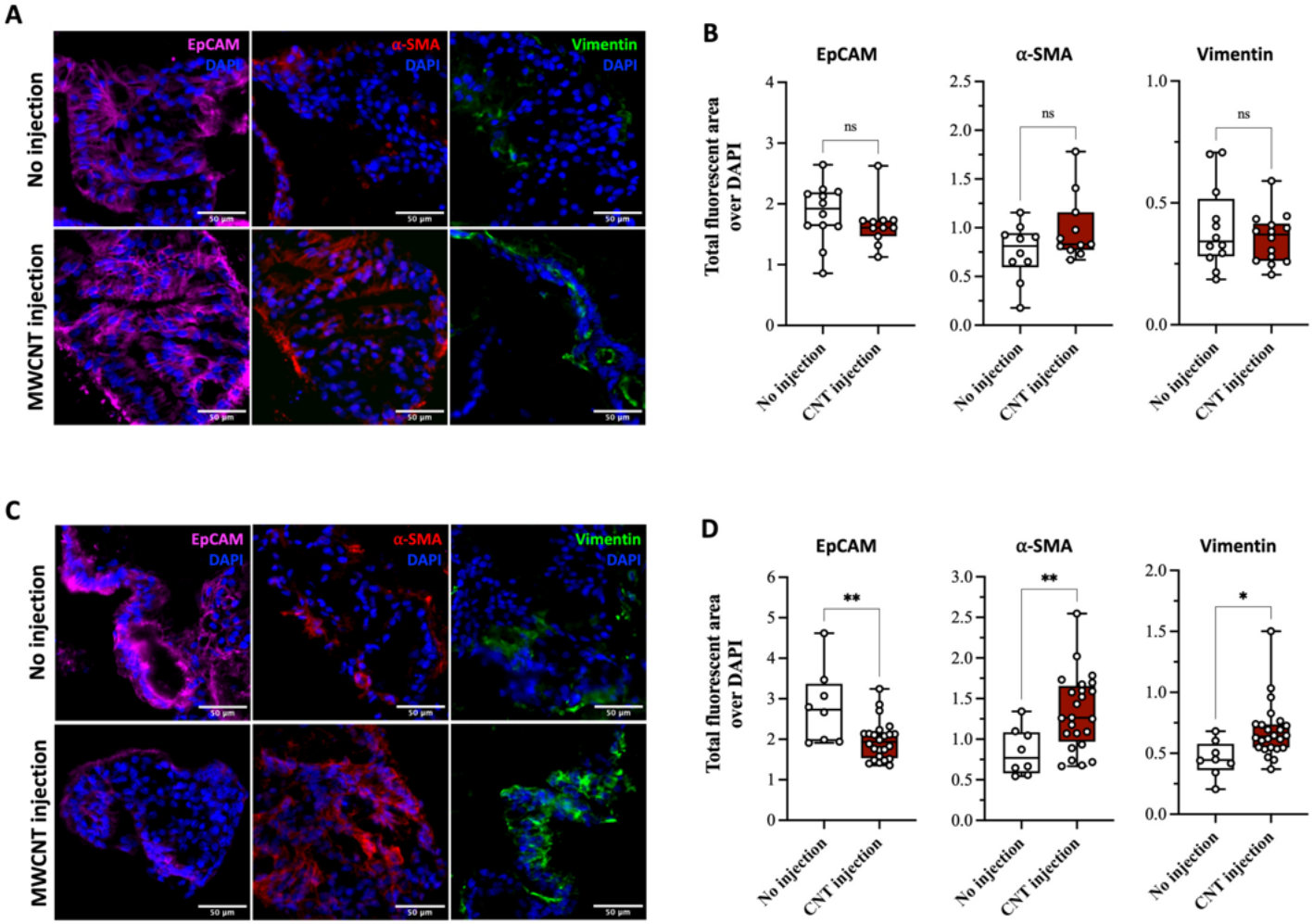

Figure 6. MWCNT-induced fibrosis in lung organoids after 1d and 7d exposure to mid dose MWCNT. A-B, 1d exposure. **C-D,** 7d exposure. **A and C**, Immunofluorescence micrographs of lung organoid sections stained for epithelial (EpCAM) and mesenchymal (α-SMA, vimentin) markers after MWCNT exposure. **B and D**, Semi-quantitative analysis showing the change in the expression of the indicated epithelial (EpCAM) and mesenchymal (α-SMA, vimentin) markers after MWCNT exposure. Boxplots represent the median, with whiskers indicating minimum and maximum of data (n = 8 to 24 independent images, from 3 experiments). Unpaired two-tailed Student's t-test. ns = not significant, $*P < 0.05$, $**P < 0.01$.

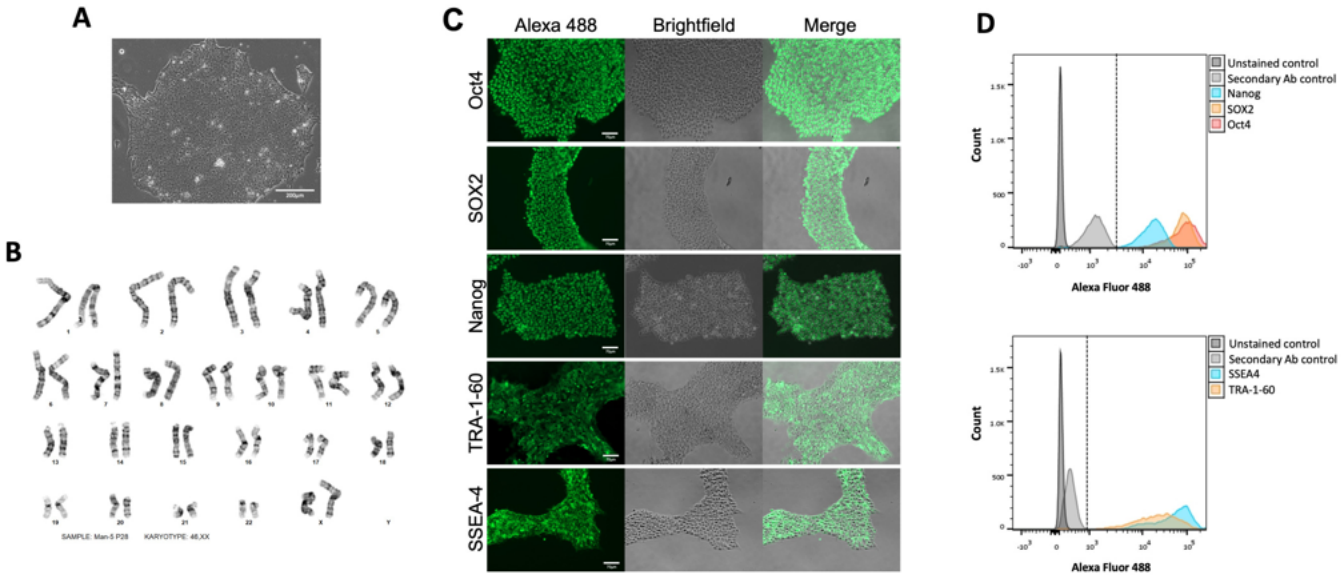

Figure S1. Pluripotency assessment of hESC line Man5. A, Brightfield image of hESC line Man5 after culturing to confluence. **B,** G-banded karyotyping of P28 Man5 cells. **C**, Immunofluorescence micrographs of Man5 cells stained for markers of pluripotency. **D,** Representative flow cytometry profile of Man5 cells stained for intracellular (top panel) and cell surface (bottom panel) markers of pluripotency.

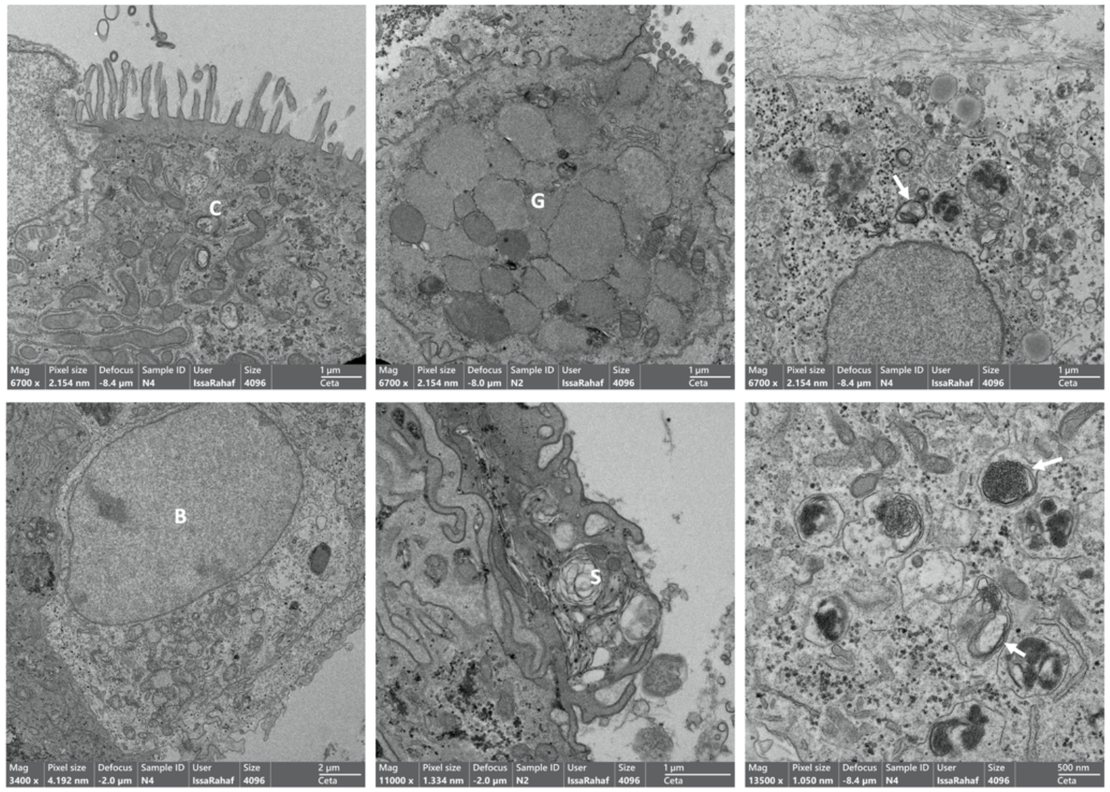

Figure S2. Transmission electron microscopy images of d63 lung organoids. C, Multi-ciliated cell. G, goblet cell. B, basal cell. S, surfactant deposition. Arrows indicate cell with mature lamellar bodies, the organelles in which surfactant is stored before exocytosis.

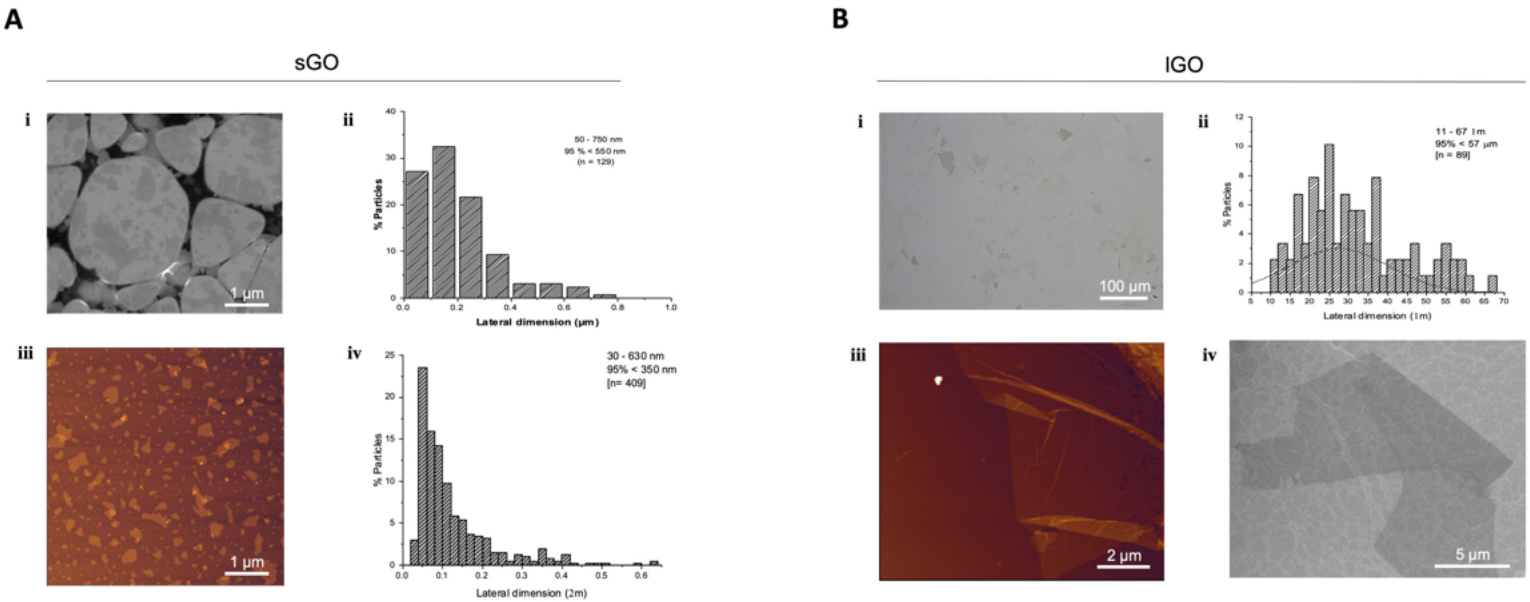

Figure S3. Physiochemical characterisation of representative lGO and sGO sheets. A, sGO sheets. **B,** lGO sheets. (Ai) Scanning electron micrograph of sGO and (Aii) the corresponding lateral dimension distribution. (Aiii) Height atomic force micrograph and (Aiv) the corresponding lateral dimension distribution. (Bi) Optical micrograph of lGO sheets and (Aii) the corresponding lateral dimension distribution. (Aiii) Height atomic force micrograph and (Aiv) scanning electron micrograph of lGO.

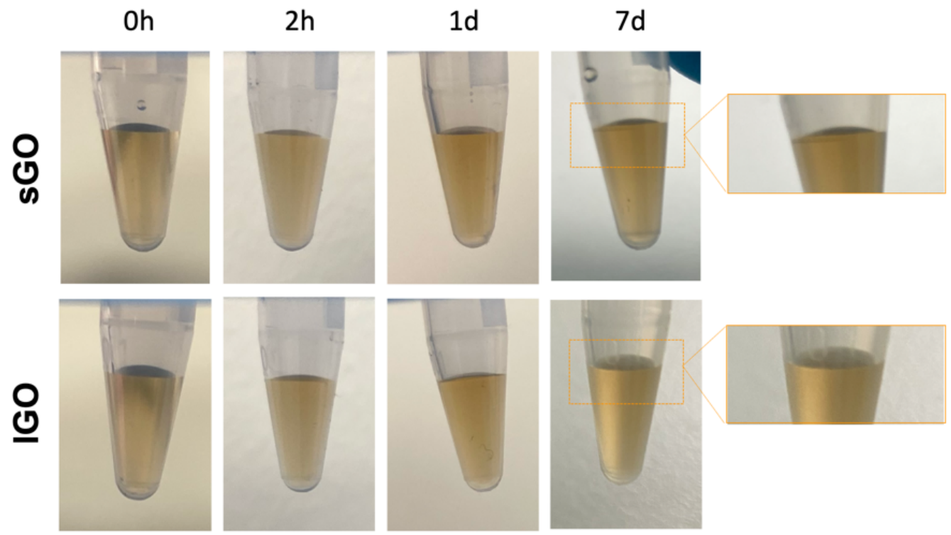

Figure S4. Stability of sGO and lGO in microinjection buffer, PBS$^{-/-}$. Materials were prepared at 0.2 mg/ml in microinjection buffer (PBS$^{-/-}$). Preparations were examined for signs of agglomeration after 0h and 2h at room temperature, and after 1d and 7d at 37°C, 5% CO_2

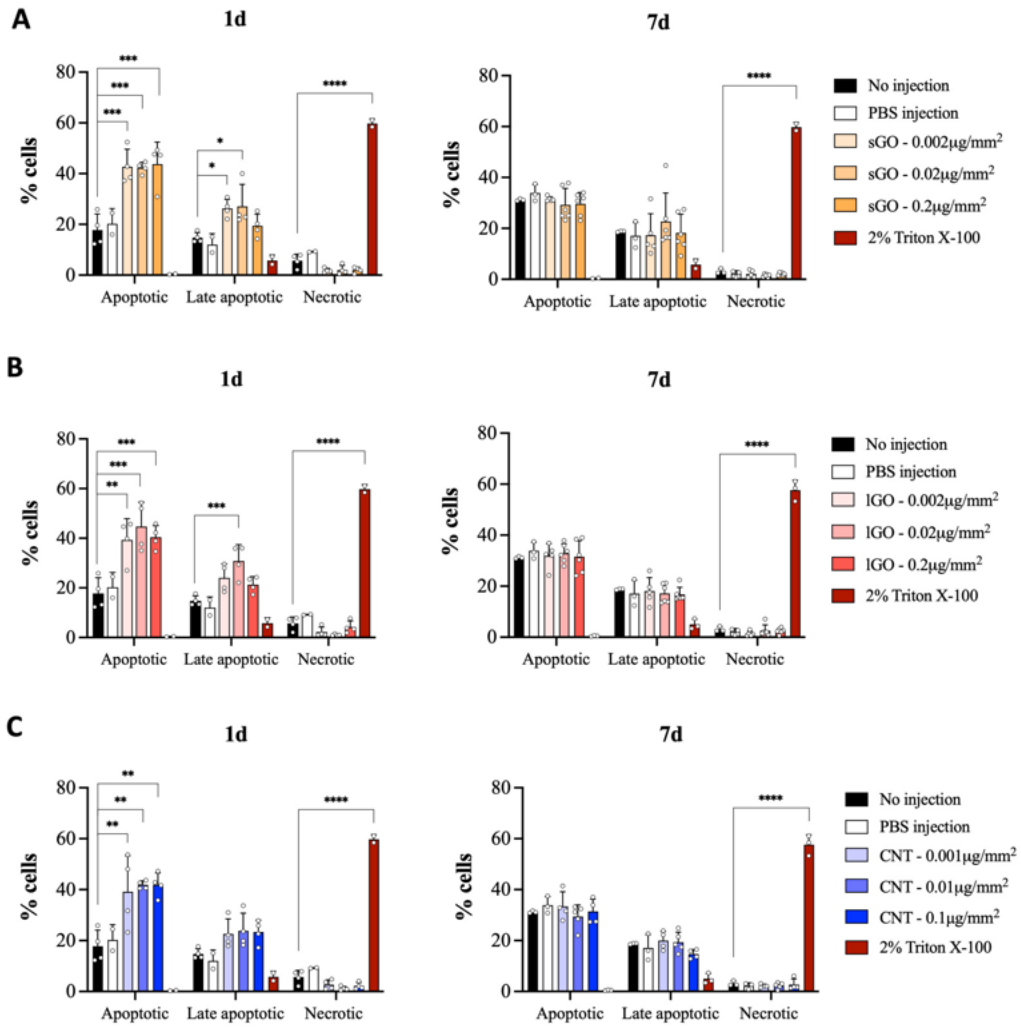

Figure S5. Viability of human lung organoids after 1d and 7d exposure to carbon-based NM. A, sGO exposure. **B,** lGO exposure. **C,** MWCNT exposure. After exposure, organoids were dissociated into single cells, stained with Annexin V/propidium iodide and analysed using flow cytometry. Cells staining AV+PI-, AV+PI+ and AV-PI+ were considered apoptotic, late apoptotic and necrotic, respectively. Representative flow cytometric dot plots and the gating strategy are shown in Figure S6. Data represent the mean ±SD (n = 4, 6-8 organoids per replicate). One-way ANOVA. $^{**}P < 0.01$, $^{**}P < 0.001$, $^{****}P < 0.0001$.

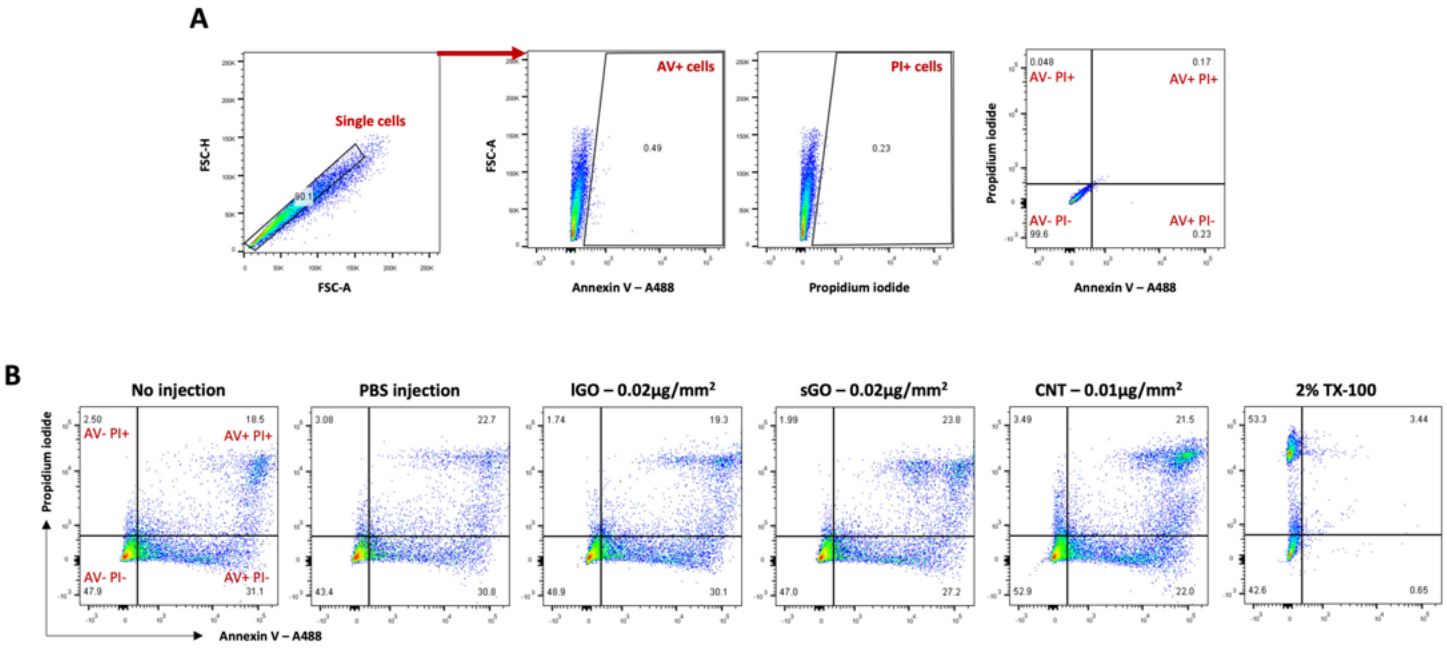

Figure S6. Viability of Man5-derived human lung organoids after 7d exposure to carbon-based material. A, Gating strategy implemented for the analysis of lung organoid dissociated cells (data shows the unstained-untreated control). **B,** Representative flow cytometry dot plots of annexin V/propidium iodide stained lung organoids after exposure to carbon-based NM for 7d.

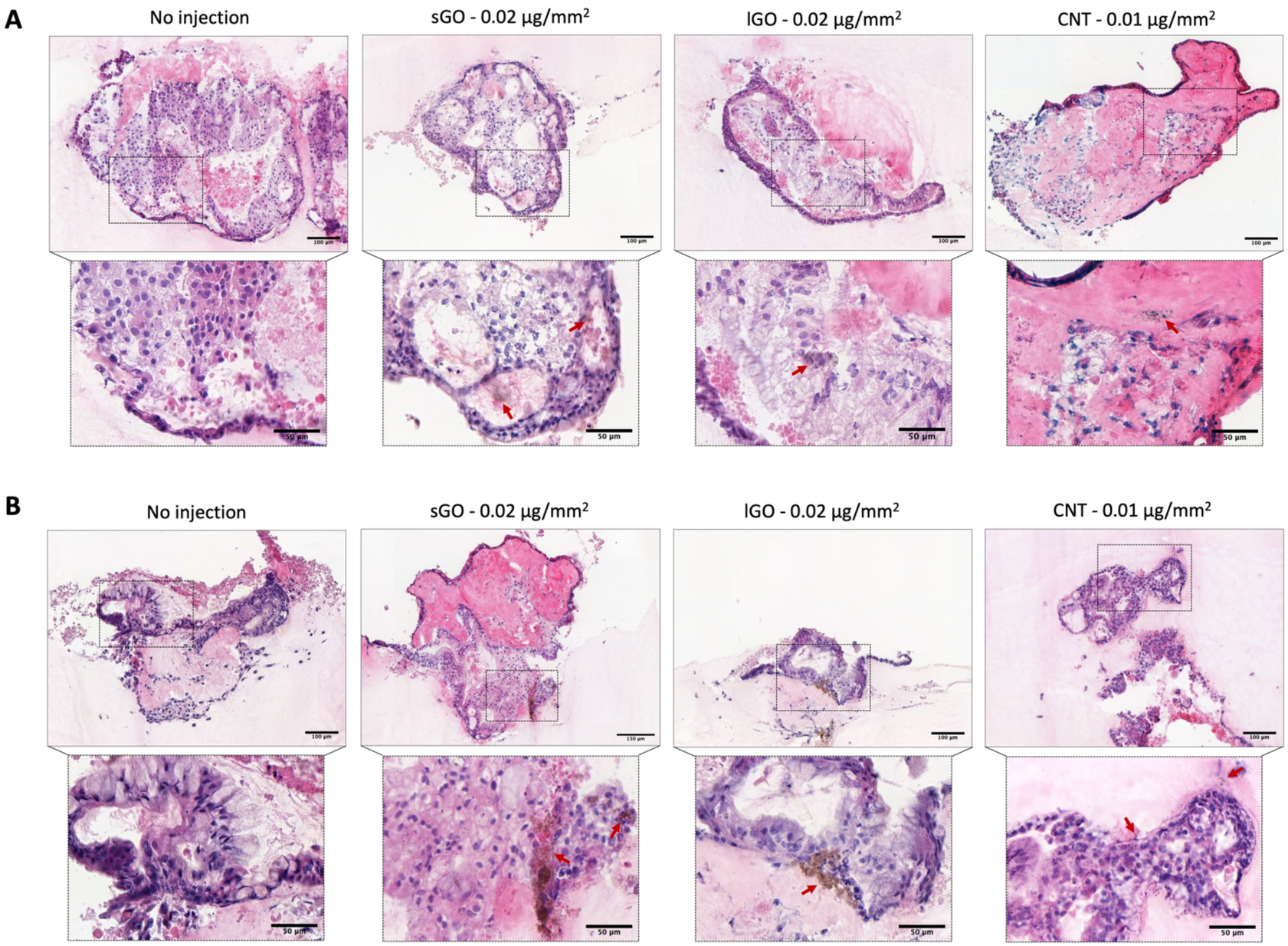

Figure S7. Histological analysis of Man5-derived human lung organoids after 1d and 7d exposure to mid dose of carbon-based material. A, 1d exposure. **B,** 7d exposure. Organoids were flash-frozen, cryo-sectioned at a thickness of 10 µm and stained with H&E. Arrows indicate material localisation.

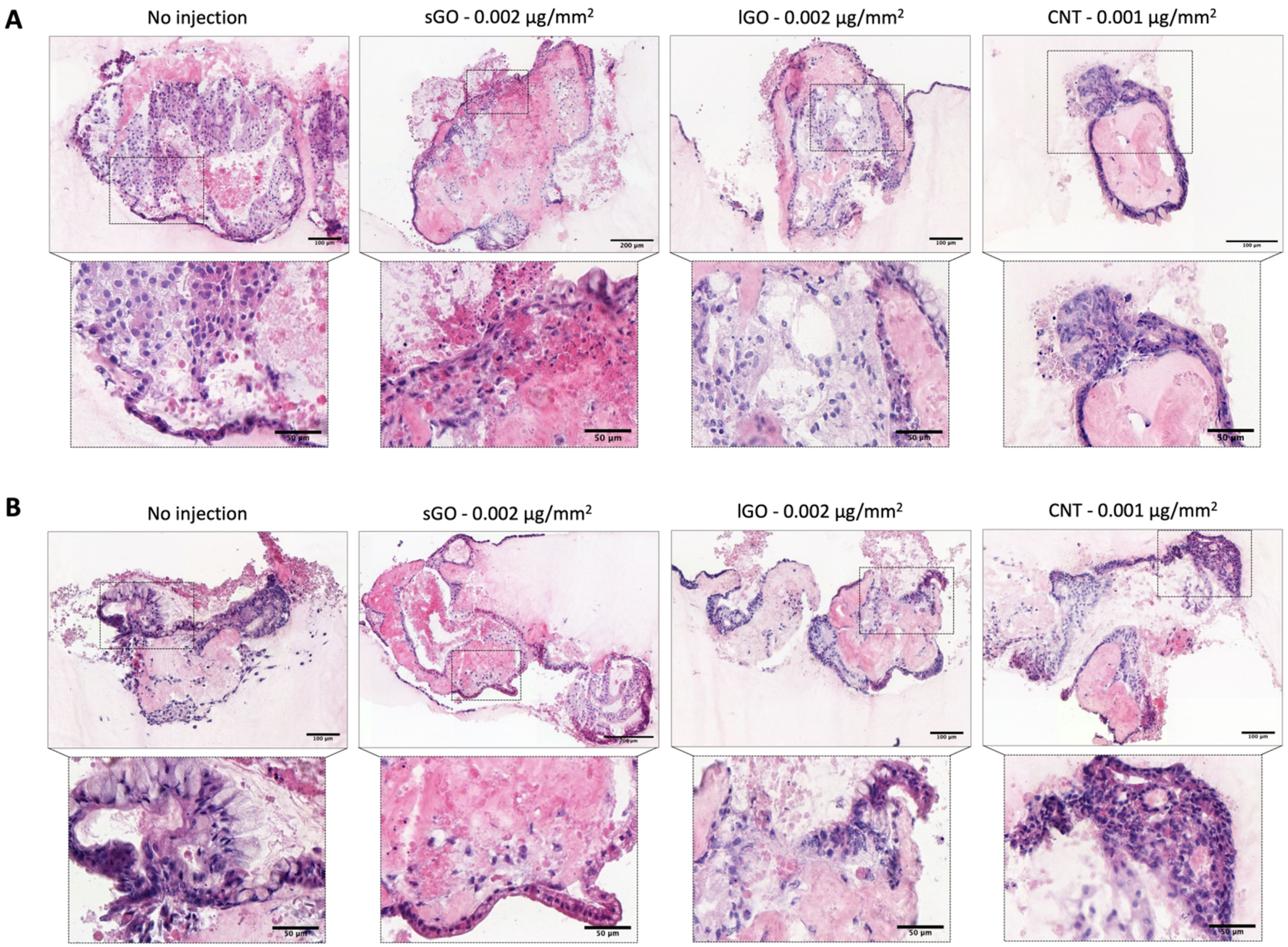

Figure S8. Histological analysis of Man5-derived human lung organoids after 1d and 7d exposure to low dose of carbon-based material. A, 1d exposure. **B,** 7d exposure. Organoids were flash-frozen, cryo-sectioned at a thickness of 10 µm and stained with H&E. Arrows indicate material localisation.

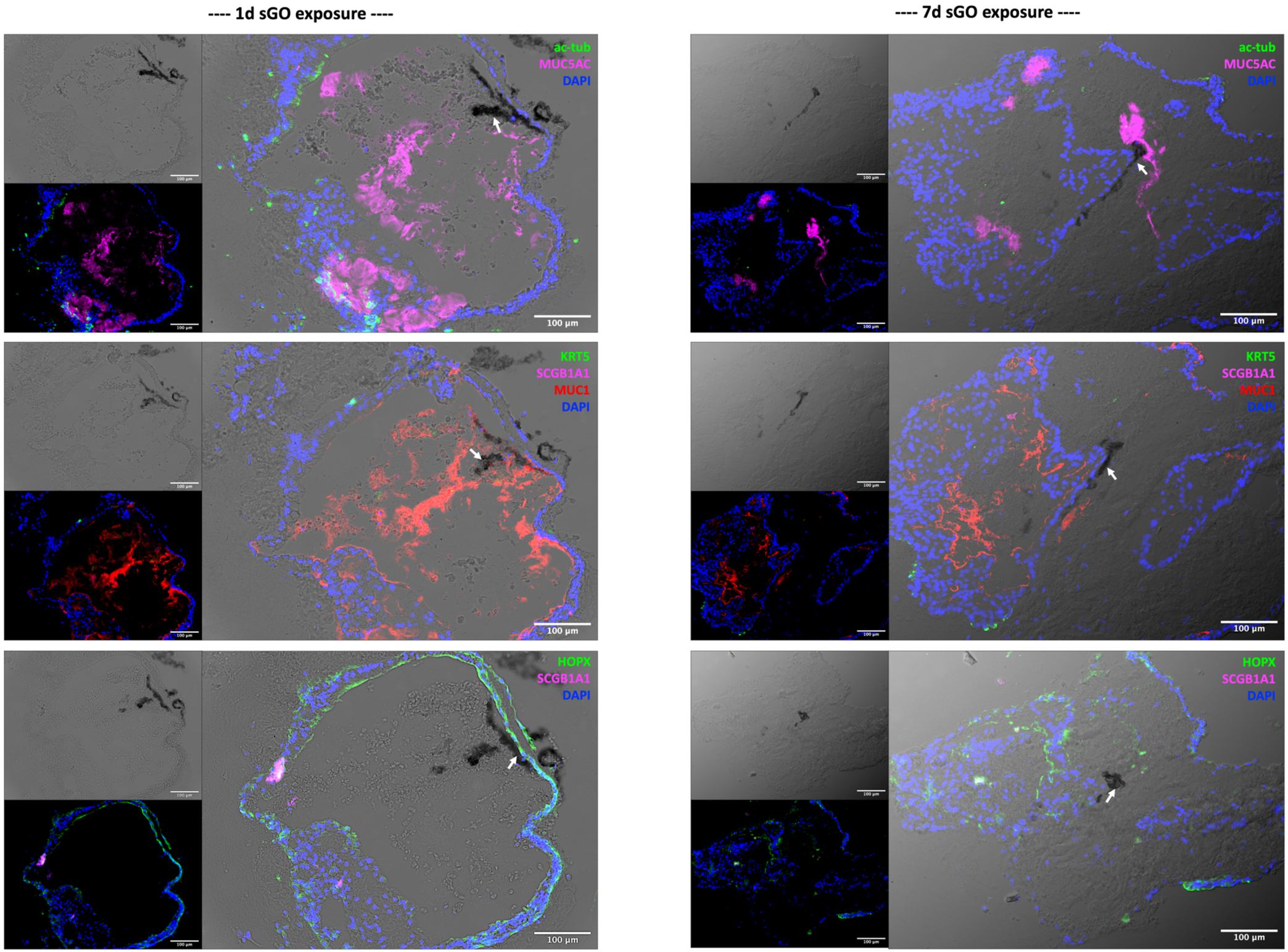

Figure S9. Limited interaction of sGO with proximal airway cells. A, 1d exposure. **B,** 7d exposure. After material exposure, organoids were cryo-sectioned at thickness of 10 µm and immuno-stained for markers of proximal and distal airway epithelial cells. sGO dose, 0.2 µg/mm^2. Proximal airway cell markers: ac-tub (marker for ciliated cells); KRT5 (basal cells); SCGB1A1 (club cells); MUC5AC (goblet cells when associated to organoid epithelium, or secretory mucin when present in the luminal space). Distal airway cell markers: HOPX (marker for AECI cells); MUC1 (AECII cells when associated to organoid epithelium, or secretory mucin when present in the luminal space). Arrows indicate material localisation. Scale bar, 100 µm.

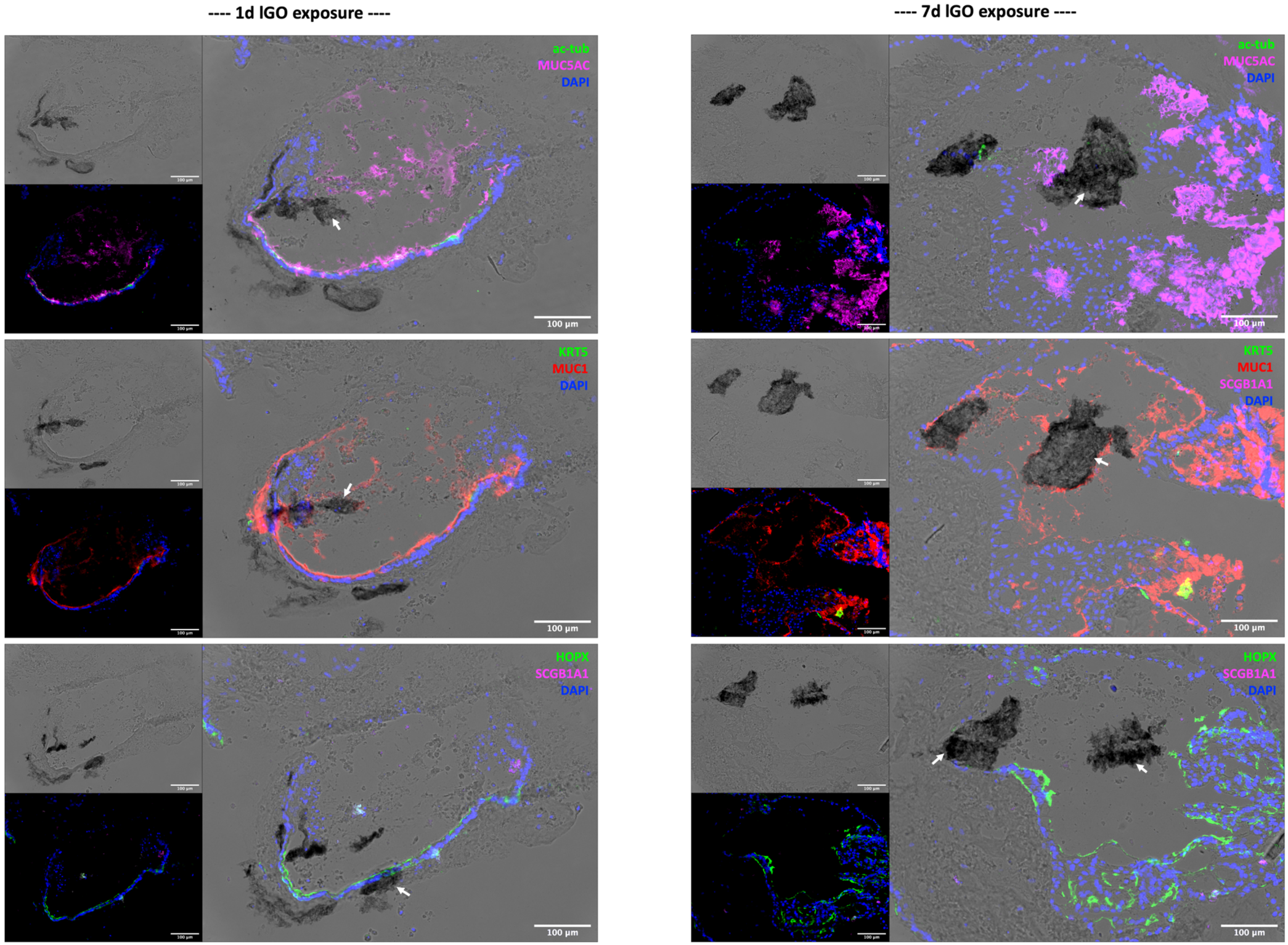

Figure S10. Limited interaction of lGO with proximal airway cells. A, 1d exposure. **B,** 7d exposure. After material exposure, organoids were cryo-sectioned at thickness of 10 µm and immuno-stained for markers of proximal and distal airway epithelial cells. lGO dose, 0.2 µg/mm^2. Proximal airway cell markers: ac-tub (marker for ciliated cells); KRT5 (basal cells); SCGB1A1 (club cells); MUC5AC (goblet cells when associated to organoid epithelium, or secretory mucin when present in the luminal space). Distal airway cell markers: HOPX (marker for AECI cells); MUC1 (AECII cells when associated to organoid epithelium, or secretory mucin when present in the luminal space). Arrows indicate material localisation. Scale bar, 100 µm.

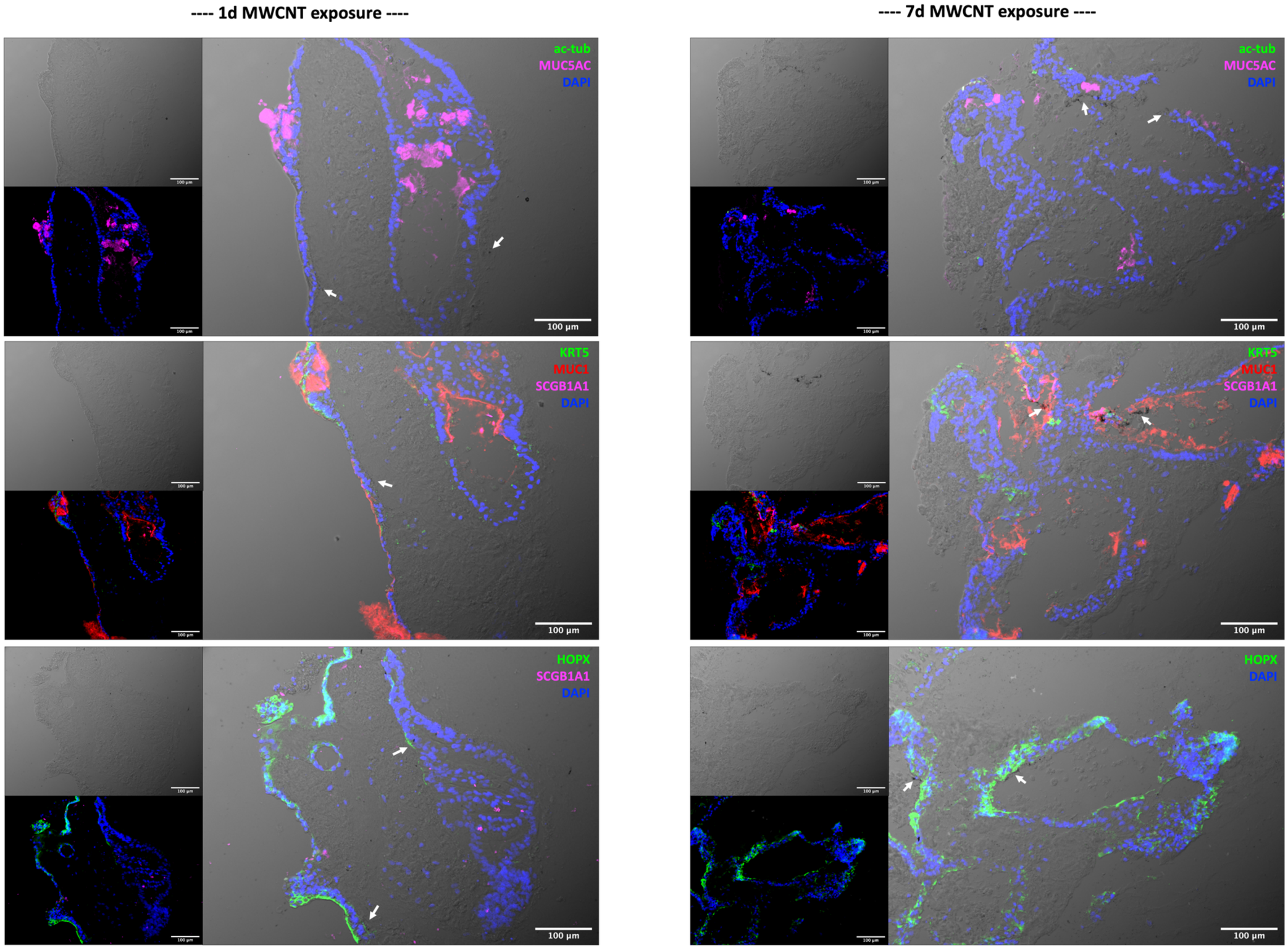

Figure S11. Limited interaction of MWCNT with proximal airway cells. A, 1d exposure. **B,** 7d exposure. After material exposure, organoids were cryo-sectioned at thickness of 10 µm and immuno-stained for markers of proximal and distal airway epithelial cells. MWCNT dose, 0.01 µg/mm^2. Organoids exposed to a mid dose of MWCNT were used to assess material-cell interaction due to the detrimental impact of MWCNT on the organoid, when sectioning at high material load. Proximal airway cell markers: ac-tub (marker for ciliated cells); KRT5 (basal cells); SCGB1A1 (club cells); MUC5AC (goblet cells when associated to organoid epithelium, or secretory mucin when present in the luminal space). Distal airway cell markers: HOPX (marker for AECI cells); MUC1 (AECII cells when associated to organoid epithelium, or secretory mucin when present in the luminal space). Arrows indicate material localisation. Scale bar, 100 µm.

SUPPLEMENTARY MATERIAL

RESULTS

HLO development and characterisation. Immunofluorescence analysis, **Figure 1I** revealed that basal ($KRT5^+$) and club ($SCGB1A1^+$) cells are interspaced throughout the organoid, whilst ciliated ($acTUB^+$) and goblet cells ($MUC5AC^+$) appear in clusters (with secreted mucin accumulating in the luminal space). Markers occurred in epithelial structures that appeared polarised, with $KRT5^+$ cells on the basal side and $acTUB^+$ on the apical side. Distal AECII cells expressing SFTPB, SFTPC and MUC1 were abundant in the culture. Markers of AECI such as HOPX were found in areas of cell flattening and thinning of the cultures and exhibited thin cytoplasmic extensions, which is a morphological characteristic of AECI *in vivo* cells.

s/lGO and MWCNT exposure does not permanently impact organoid viability. Cytotoxicity is a key endpoint when evaluating the toxicological profile of NMs. To assess the impact of injection and material exposure on organoid viability, we dissociated the organoids into single cells after s/lGO, MWCNT or PBS exposure and analysed the cells using the AV/PI flow cytometry assay. We included organoids exposed to PBS-alone to determine if puncture with the microinjection needles induces any mechanical trauma that may impact organoid viability. We also included organoids exposed to 2% Triton X-100 as a positive control for cell death. All three materials induced a short-lived apoptotic response that did not progress to late apoptosis or necrosis **(Figures 3A-3C)**. At the highest dose tested for s/lGO and MWCNT, ~20% more cells stained positive for markers of early apoptosis (AV^+PI^-) after 1d exposure when compared to the non-injected control. Furthermore, there was limited/no evidence of late apoptotic (AV^+PI^+) or necrotic (AV^-PI^+) cells after 1d material exposure. We did not observe a dose-dependent effect, suggesting that material-induced toxicity at 1d exposure may be limited to a few cell types within the organoids. The effects observed were not due to mechanical trauma as there was no significant difference between the non-injected and PBS-injected controls after both 1 and 7d exposure. Interestingly, after 7d exposure there was no evidence of any cell death (apoptosis, late apoptosis, or necrosis) in all material exposure groups. Taken together, these results suggest that lung organoids can withstand material exposure and have the capability to recover from the initial impact of NM exposure.

Table S1. Primary antibodies used for immunostaining.

ANTIBODY	MANUFACTURER (CATALOGUE NO.)	DILUTION FACTOR
acTUB	Cell Signalling Technology (#5335)	1:400
α-SMA	Abcam (#ab5694)	1:300
EpCAM	Biolegend (#324202)	1:500
FOXA2 (HNF-3a)	R&D systems (#AF2400)	1:20
HOPX	Proteintech (#11419-1-AP)	1:100
KRT5	Thermo Scientific (#MA5-14473)	1:200
MUC1	Thermo Scientific (#MA5-11202)	1:200
MUC5AC	Thermo Scientific (#MA5-12178)	1:200
Nanog	Abcam (#ab106465)	1:100
NKX2.1	Thermo Scientific (#MA5-13961)	1:40 (adherent cells); 1:100 (cryosections)
Oct.4	Abcam (#ab19857)	1:500
SCGB1A1 (CC10)	R&D systems (#MAB4218)	1:100
SSEA-4	Abcam (#ab16287)	1:100
SFTPB (Mature)	Seven Hills (#WRAB-48604)	1:1000
SFTPC (Mature)	Seven Hills (#WRAB-76694)	1:500
SOX2	BD Bioscience (#561469)	1:50
SOX9	Sigma Aldrich (#AB5535)	1:200 (adherent cells); 1:300 (cryosections)
TRA-1-60	Abcam (#ab16288)	1:100
Vimentin	Abcam (#ab24525)	1:400

Table S2. Secondary antibodies used for immunostaining.

ANTIBODY	MANUFACTURER (CATALOGUE NO.)	DILUTION FACTOR
Donkey anti-goat 488	Thermo Scientific (#A11055)	1:500
Donkey anti-rabbit 488	Thermo Scientific (#A21206)	1:500 (adherent cells); 1:200 (flow cytometry); 1:400 (cryosections)
Donkey anti-mouse 647	Thermo Scientific (#A31571)	1:400
Goat anti-chicken 488	Thermo Scientific (#A11039)	1:400
Goat anti-mouse 488	Thermo Scientific (#A11001)	1:500 (adherent cells); 1:200 (flow cytometry); 1:400 (cryosections)
Goat anti-rabbit 488	Thermo Scientific (#A11034)	1:400
Goat anti-hamster 568	Abcam (#ab175716)	1:400
Goat anti-rabbit 594	Thermo Scientific (#A11012)	1:400
Goat anti-mouse 647	Thermo Scientific (#A21236)	1:400
Goat anti-rat 647	Thermo Scientific (#A21247)	1:400

Table S3. Antibodies used for flow cytometry.

ANTIBODY	CONJUGATE	MANUFACTURER (CATALOGUE NO.)	DILUTION FACTOR
cKIT	PE	Biolegend (#313204)	1µl/2x10^5 cells
CXCR4	APC	Biolegend (#306510)	1µl/2x10^5 cells
EpCAM	AF488	Biolegend (#324210)	1µl/2x10^5 cells
MUC1	APC	Biolegend (#337004)	1µl/2x10^5 cells
Nanog	Uncojugated	Thermo Scientific (#MA1-017)	1:200
Oct.4	Unconjugated	Abcam (#ab19857)	1:500
PDNP	PE	Biolegend (#355608)	1µl/2x10^5 cells
SSEA-4	Unconjugated	Abcam (#ab16287)	1:500
SOX2	Unconjugated	BD Bioscience (#561469)	1:200
TRA-1-60	Unconjugated	Abcam (#ab16288)	1:500